

Endo-exo framework for a unifying classification of episodic landslide movements

Qinghua Lei^{1,*}, Didier Sornette²

¹*Department of Earth Sciences, Uppsala University, Uppsala, Sweden*

²*Institute of Risk Analysis, Prediction and Management, Academy for Advanced Interdisciplinary Studies, Southern University of Science and Technology, Shenzhen, China*

Abstract

Landslides exhibit intermittent gravity-driven downslope movements developing over days to years before a possible major collapse, commonly boosted by external events like precipitations and earthquakes. The reasons behind these episodic movements and how they relate to the final instability remain poorly understood. Here, we develop a novel “endo-exo” theory to quantitatively diagnose landslide dynamics, capturing the interplay between exogenous stressors such as rainfall and endogenous damage/healing processes. We predict four distinct types of episodic landslide dynamics (endogenous/exogenous-subcritical/critical), characterized by power law relaxations with different exponents, all related to a single parameter ϑ . These predictions are tested on the dataset of the Preonzo landslide, which exhibited multi-year episodic movements prior to a catastrophic collapse. All its episodic activities can be accounted for within this classification with $\vartheta \approx 0.45 \pm 0.1$, providing strong support for our parsimonious theory. We find that the final collapse of this landslide is clearly preceded over 1-2 months by an increased frequency of medium/large velocities, signaling the transition into a catastrophic regime with amplifying positive feedbacks.

Main text

Landslides, a widespread form of mass wasting, occur in various Earth surface environments and pose significant threats to life and property worldwide^{1,2}. Due to rapid population growth and urbanization, human habitats are increasingly exposed to landslide hazards, with the situation becoming even more severe under climate change, where extreme rainfall, permafrost thaw, and glacier retreat have promoted fatal landslides³. Extensive field observations show that landslides commonly exhibit episodic movements characterized by intermittent acceleration-deceleration sequences that are boosted by external events like precipitations and earthquakes⁴⁻¹². Some landslides have episodically crept over hundreds or thousands of years, while others could evolve into a major collapse after episodically deforming over days to years¹³. The reasons behind these episodic movements (marked by intermittent bursts of displacement activities followed by sustained periods of relaxation dynamics) and how they relate to a possible final catastrophic failure remain poorly understood, inhibiting our capability to predict landslide behavior and mitigate the associated risks.

We identify the following fundamental questions: (a) Are episodic landslide movements of an exogenous or endogenous origin? (b) What are their underlying mechanisms? (c) How do they relate to catastrophic failures? Here, we address these questions by establishing a novel “endo-exo” theoretical framework to quantitatively diagnose episodic landslide movements by analyzing the

* Corresponding author: qinghua.lei@geo.uu.se

precursory/recovery properties of intermittent velocity peaks. This allows us to classify episodic landslide movements into four distinct types as well as to decipher their endogenous/exogenous origins and triggering mechanisms. Our theory is very parsimonious with a single adjustable parameter accounting for all the four power law regimes of episodic landslide dynamics. We provide a thorough demonstration of our theory based on the long-term monitoring dataset of a rainfall-induced landslide at Preonzo, Switzerland, which episodically moved over many years prior to a major collapse. We observe all the four types of episodic dynamics in the Preonzo landslide with their precursory/recovery properties consistent with our theoretical prediction. Finally, we provide predictive insights into the transition of this landslide from episodic to catastrophic regimes, which is clearly preceded over 1-2 months by a notable decline in the power law exponent of the probability distribution of slope velocities. This finding opens up a new avenue for forecasting catastrophic landslides.

Results

Model of self-excited triggered mass movements. We conceptualize a landslide as a complex system consisting of numerous geomaterial masses interacting via cohesive or frictional contacts. The displacement activity of the landslide results from a combination of external forces like precipitations and earthquakes, and of internal influences where each past moved mass may prompt other masses in its network of interactions to move as a result of the redistribution of mechanical stress, pore pressure, and possibly other physico-chemical fields. This impact of a mass on other masses is not instantaneous, due to the time-dependent nature of the relevant geomechanical processes like creep, damage, and friction¹⁴. This latency can be described by a memory kernel $\psi(t - \tau)$, giving the probability that the movement of a mass at time τ leads to the movement at a later time t by another mass in direct interaction with the first moved mass. This memory kernel $\psi(t - \tau)$ can be seen as a fundamental macroscopic description of how long it takes for a mass to be triggered to move following the interaction with an already moved neighboring mass. In other words, it is a “bare” propagator, describing the distribution of waiting times between “cause” and “action” for a mass to move, which may obey a power law characterizing a long-memory process^{15,16}:

$$\psi(t - \tau) \propto 1/(t - \tau)^{1+\vartheta}, \text{ with } 0 < \vartheta < 1 \text{ and for } t - \tau > c \quad (1)$$

where the exponent ϑ controls the persistence of memory and c is a small characteristic time scale regularizing the singularity at $t - \tau = 0$. For instance, one way to implement the regularization is to replace $1/(t - \tau)^{1+\vartheta}$ by $1/(t - \tau + c)^{1+\vartheta}$. Such a regularization is essential to make the integral of $\psi(t)$ finite and thus ensure a valid theory. Physically, this ensures the finiteness of the number of mass movements triggered by a preceding one. The assumption that $\psi(t)$ has a power law tail is supported by many empirical observations such as Andrade’s law of material creep¹⁷ and Omori’s law of aftershock activity¹⁸.

Starting from an initial moved mass, i.e., the “mother” mass, which first displaces due to either external forces or internal fluctuations, it may trigger the movements of first-generation “daughter” masses nearby, which themselves trigger their own daughter masses to move, and so on. Such an epidemic process can be captured by a conditional self-excited point process¹⁹, which can be mapped exactly onto a branching process, such that the average of the displacement rate (i.e., velocity) of the mass system is governed by the following self-consistent equation^{16,20}:

$$v(t) = V(t) + n \int_{-\infty}^t \psi(t - \tau) v(\tau) d\tau, \quad (2)$$

where $V(t)$ is the exogenous source that is not triggered by any epidemic effect in the system and $n \geq 0$ is the effective branching ratio defined as the average number of moving daughter masses triggered by a mother mass that moved in the past. Equation (2) is the equation for the first-order moment (or average) of the velocity, whose underlying dynamics is given by a self-excited point process. The branching ratio n depends on the network topology of geomaterial masses and the spreading behavior of disturbances in the system, therefore reflecting the maturation of the landslide, with $n < 1$, $n \simeq 1$, and $n > 1$ corresponding to the subcritical, critical, and supercritical regimes, respectively^{21,22}. Here, we mainly focus on the subcritical and critical regimes with $n \lesssim 1$ to ensure stationarity, whereas the transition into the supercritical regime $n > 1$ related to the emergence of a catastrophic failure^{23,24} will be explored in the Discussion section.

Classifications of episodic landslide dynamics. According to our model and derivations (see Methods), landslide velocities around a peak at time t_c can be described by a generalized finite-time singularity power law as:

$$v(t) \propto 1/|t - t_c|^p, \quad (3)$$

where the exponent p depends on the parameter ϑ and the regime delineated by a characteristic time t^* given by²³:

$$t^* = c \left(\frac{n\Gamma(1-\vartheta)}{|1-n|} \right)^{1/\vartheta} \propto |1-n|^{-1/\vartheta}, \quad (4)$$

such that, as $n \rightarrow 1$ (critical regime), $t^* \rightarrow +\infty$, so that the short-term response prevails ($t - t_c < t^*$); as $n \rightarrow 0$ (pure noncritical regime), $t^* \rightarrow c$ and the long-term response dominates ($t - t_c > t^*$); if $0 < n < 1$ (subcritical regime), t^* has a finite value and the system may manifest a coexistence of both short- and long-term responses. This allows us to classify episodic landslide movements into four fundamental types based on a combination of the origin of disturbance (exogenous/endogenous) and the cascading behavior (subcritical/critical)²⁵:

- Type I: Exogenous-subcritical, with $p = 1 + \vartheta$ for $t - t_c > t^*$. Here, the system is not “ripe” and the cascading propensity is limited ($n < 1$), meaning that the exogenously induced displacement activity at time t_c does not cascade beyond the first few generations of triggered masses. The post-peak velocity relaxation is thus governed by the bare memory kernel.
- Type II: Exogenous-critical, with $p = 1 - \vartheta$ for $c < t - t_c < t^*$. Here, the system is ripe ($n \simeq 1$), such that the exogenously induced displacement activity at time t_c cascades through the system of interconnected masses, triggering neighboring masses that further trigger their own neighboring masses and so on. The post-peak velocity relaxation is governed by the “dressed” memory kernel (see Methods).
- Type III: Endogenous-subcritical, with $p = 0$ for $|t - t_c| > t^*$. The displacement activity does not result from an exogenous event but instead from an endogenous forcing. The system is not ripe ($n < 1$) such that no cascade develops and the (small) peak is associated with no apparent precursory/recovery signatures.
- Type IV: Endogenous-critical, with $p = 1 - 2\vartheta$ for $c < |t - t_c| < t^*$. The displacement activity originates from endogenous growth/interaction within the ripe system ($n \simeq 1$), where the triggering cascades produce an approximately symmetrical power law acceleration-deceleration behavior around the peak.

This classification arises from the interplay of the bare long-memory process as embodied in equation (1) and the epidemic cascade throughout the system as captured by equation (2). It can be seen that the relaxation following an endogenous-critical peak (with a smaller exponent $p = 1 - 2\vartheta$) is slower than that following an exogenous-critical peak (with a larger exponent $p = 1 - \vartheta$). This longer-lived influence of an endogenous-critical peak results from the precursory process that impregnates the system much more than its exogenous counterpart²⁶.

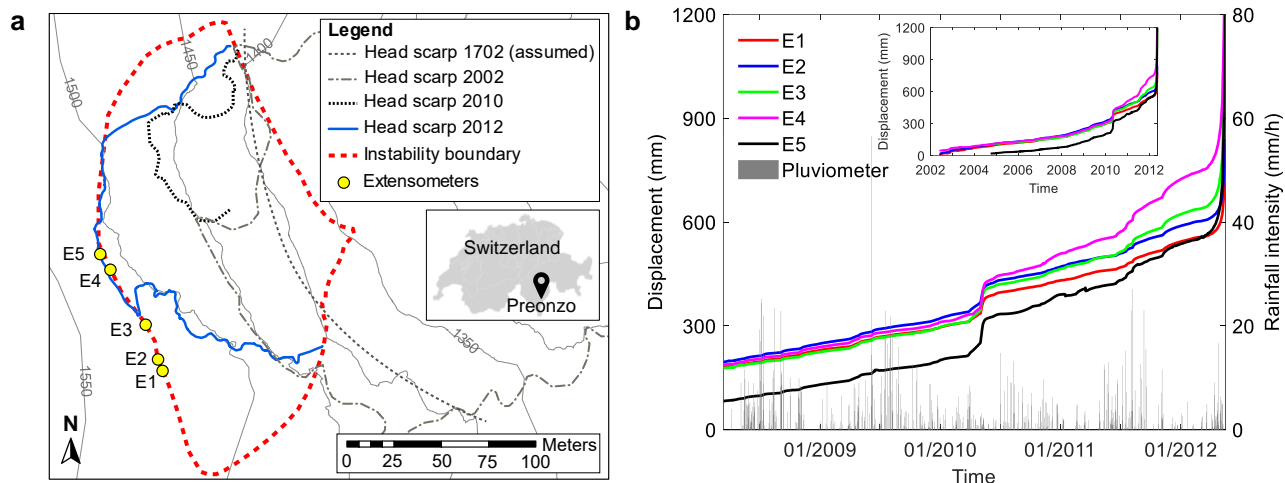


Fig. 1 Preonzo landslide, Switzerland. **a** Overview of the landslide site with the locations of five extensometers E1-E5, the boundary of this instability complex, and the headscarps of historical failure events indicated. **b** Monitoring data of slope displacements by the five extensometers and recorded data of rainfall intensity by a pluviometer installed at the slope.

Application to the Preonzo landslide, Switzerland. We test our theory based on the long-term monitoring dataset of a rainfall-induced landslide at Preonzo, Switzerland²⁷, which exhibited significant episodic movements over many years prior to a catastrophic failure in 2012. This active landslide has experienced multiple failures since the 18th century²⁸ (see the headscarps of historical events in Fig. 1a). To closely monitor this instability complex that posed a great threat to the industrial and transport infrastructures located directly at the toe of the slope, five high-precision extensometers E1-E5 (see Fig. 1a for their locations) were instrumented to measure the opening of tension cracks in the headscarp area. From 2008, a pluviometer was installed to monitor the local precipitation conditions. Fig. 1b shows the time series of slope displacement measured by the five extensometers and of rainfall intensity recorded by the pluviometer between 2008 and 2012 (see the inset for the displacement time series from 2002 and Supplementary Fig. 1 for the time series of daily/cumulative rainfall amounts). One can see that this landslide exhibited a step-like deformation pattern over time as it progressively destabilized, leading up to a catastrophic failure on 15 May 2012. The displacement curve consists of numerous creep episodes (i.e., repeated cycles of accelerating-decelerating creeps) that often show a good coincidence with the occurrence of intense rainfall events.

We compute slope velocities on a daily basis from the displacement time series recorded by the five extensometers. All the four types of episodic landslide dynamics, viz., exogenous/endogenous-subcritical/critical, can be found in the velocity time series (see Figs. 2 and 3 for typical examples). We fit the data of normalized velocities to a power law (see Methods for the normalized velocity calculation and fitting algorithm).

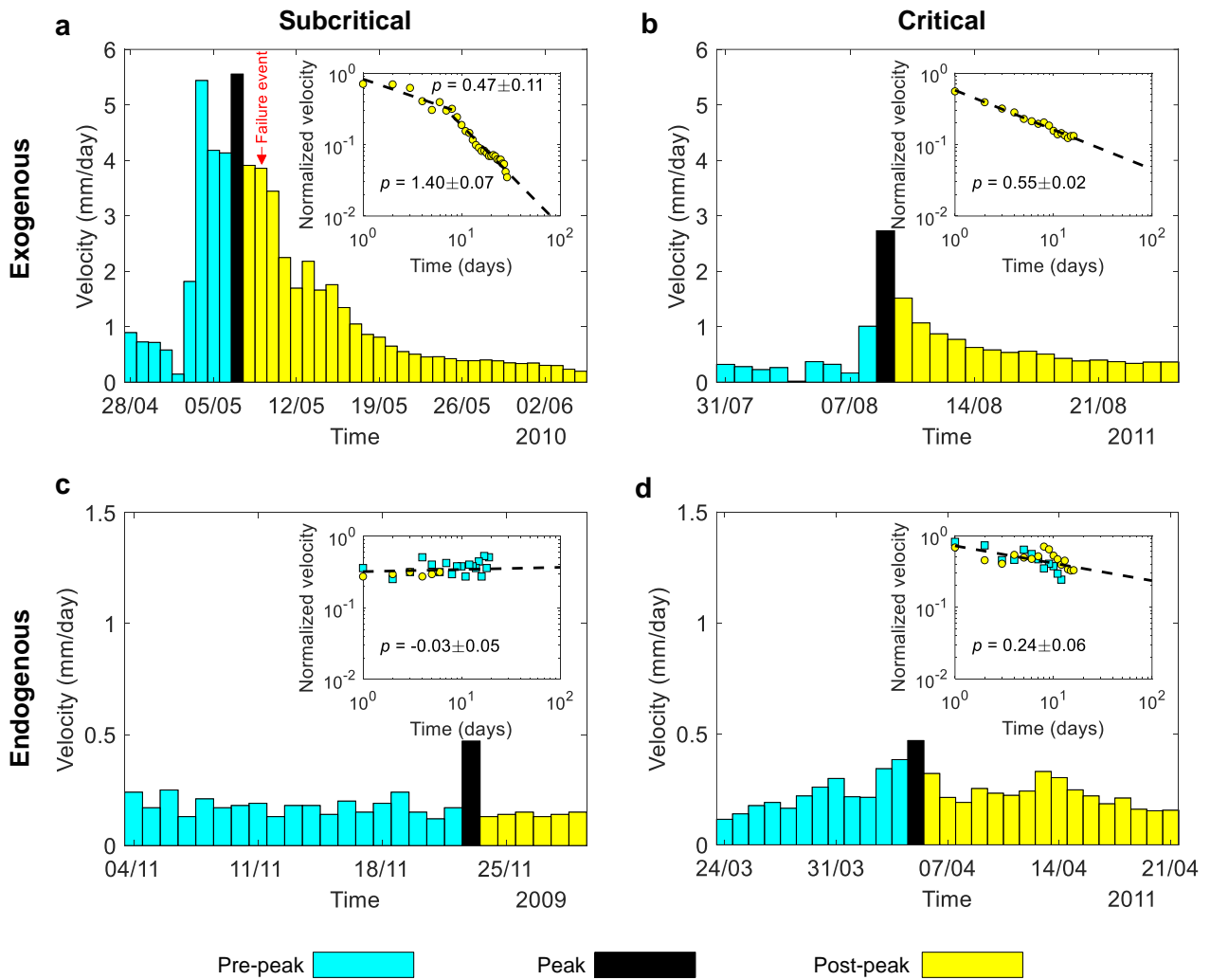


Fig. 2 Four categories of episodic landslide dynamics found in the velocity time series of the Preonzo landslide. a Type I, exogenous-subcritical; **b** Type II, exogenous-critical; **c** Type III, endogenous-subcritical; and **d** Type IV, endogenous-critical. The red arrow in **a** marks the timing of the local failure of a downslope northern sector of the slope on 9 May 2010. Insets show the post-peak relaxation of normalized velocity where dashed lines indicate the power law fitting.

For the Type I exogenous-subcritical peak on 7 May 2010 (Fig. 2a), the velocity relaxation beyond ~ 8 days after the peak is characterized by an exponent of $p = 1.40 \pm 0.07$ (exogenous-subcritical) (Fig. 2a, inset), whereas its short-term response within ~ 8 days after the peak is associated with a much smaller exponent of $p = 0.47 \pm 0.11$ (exogenous-critical), as expected from the prediction by equation (6) (see Methods). All five extensometers exhibit a similar two-branch power law relaxation behavior with an exponent of $p = 0.46 \pm 0.10$ for the short-term response and an exponent of $p = 1.54 \pm 0.06$ for the long-term response (Fig. 3a; see also Supplementary Fig. S2 for the power law fitting for individual extensometers). Around this peak accompanied by mild precipitation (Fig. 3a, left), the slope has experienced a localized failure in its northern sector downhill from the tension cracks where the extensometers are installed (see Fig. 1a for the headscarp and the Discussion section for the possible triggering mechanisms).

For the Type II exogenous-critical peak on 9 August 2011 (Fig. 2b), the post-peak velocity relaxation obeys a power law with an exponent of $p = 0.55 \pm 0.02$ (exogenous-critical) (Fig. 2b,

inset). Prior to this peak, a heavy rainstorm has occurred (Fig. 3b, left). All the five extensometers have captured this peak followed by a power law relaxation with an overall exponent of $p = 0.63 \pm 0.03$ (Fig. 3b; see also Supplementary Fig. S3 for the power law fitting for individual extensometers).

In Fig. 2c, we present a Type III endogenous-subcritical peak preceded by no rainfall event (Fig. 3c). This peak is surrounded by an essentially time-independent velocity trajectory with $p \approx 0$ (Fig. 3c), whereas most extensometers do not capture this peak and only show random fluctuations (Fig. 3c and Supplementary Fig. 4).

Lastly, we show a Type IV endogenous-critical peak (Fig. 2d), which occurs after a progressively accelerating power law growth of velocity followed by an approximately symmetrical power law relaxation, with a common exponent of $p = 0.24 \pm 0.06$. It seems that the majority of the five extensometers has captured such an approximately symmetrical precursory-recovery dynamics with a small power law exponent of $p = 0.21 \pm 0.04$ (Fig. 3d), although the timing of the peaks recorded by individual extensometers is not fully synchronized (Supplementary Fig. 5). One can notice that the time-dependent signatures of endogenous peaks are less apparent compared to exogenous ones (as reflected by the notable dispersion of the data in Figs. 2d and 3d).

Interpreting these results in light of equation (3) above, together with equations (7)-(9) (see Methods), the obtained power laws for these different peak types point to the existence of a single parameter $\vartheta \approx 0.45 \pm 0.10$, providing strong support for our theory.

We implement a peak detection algorithm to automatically extract slope velocity peaks together with their surrounding time series from the 10-year long-term monitoring dataset. We qualify a peak in the velocity time series as a local maximum over a 20-day time window which is at least $k = 2.5$ times larger than the average velocity over a 2-month time window. The time window sizes and threshold value k are chosen to give an effective detection of good-quality peaks (see Supplementary Fig. 6), but the results do not significantly change by varying these parameters (see Supplementary Figs. 7-10 and 13-14). In addition, we request that each peak has at least 10 days of post-peak data before reaching the next peak. In total, our algorithm detects 104 peaks from the entire dataset recorded by five extensometers. We then fit the post-peak velocity data of each detected peak to a power law (see Methods) over a time window ranging from 10 to 30 days, with the “best” window chosen as the one giving the highest coefficient of determination R^2 . We only keep the peaks with $R^2 > 0.8$ to extract unambiguous post-peak response functions, leaving 41 peaks. In Fig. 4a, we show the histogram of their power law exponents p , which cluster into two distinct groups, one with a median at $p \approx 0.59$ and the other with a median at $p \approx 1.52$. This result is compatible with our theoretical prediction based on $\vartheta \approx 0.45 \pm 0.10$, yielding $p \approx 1.45 \pm 0.10$ for Type I peaks and $p \approx 0.55 \pm 0.10$ for Type II peaks. It seems that Type III and IV peaks (with $p \approx 0$ and 0.1 ± 0.20 , respectively) are absent in Fig. 4a. This is because they usually have small magnitudes and considerably fluctuating post-peak responses (Fig. 2c-d and Fig. 3c-d), making it difficult for them to pass the criteria of $k = 2.5$ and $R^2 > 0.8$. We then compute the ensemble average of the relaxation behavior for the two exogenous peak types (Fig. 4b), with the fitted power laws consistent with the existence of a single parameter $\vartheta \approx 0.45 \pm 0.10$. Our results in Fig. 4 do not qualitatively change by varying the k threshold from 1.5 to 3.5 and the R^2 threshold from 0.7 to 0.9 as well as the window sizes for peak detection (Supplementary Figs. 12-14), suggesting that our method and results are robust.

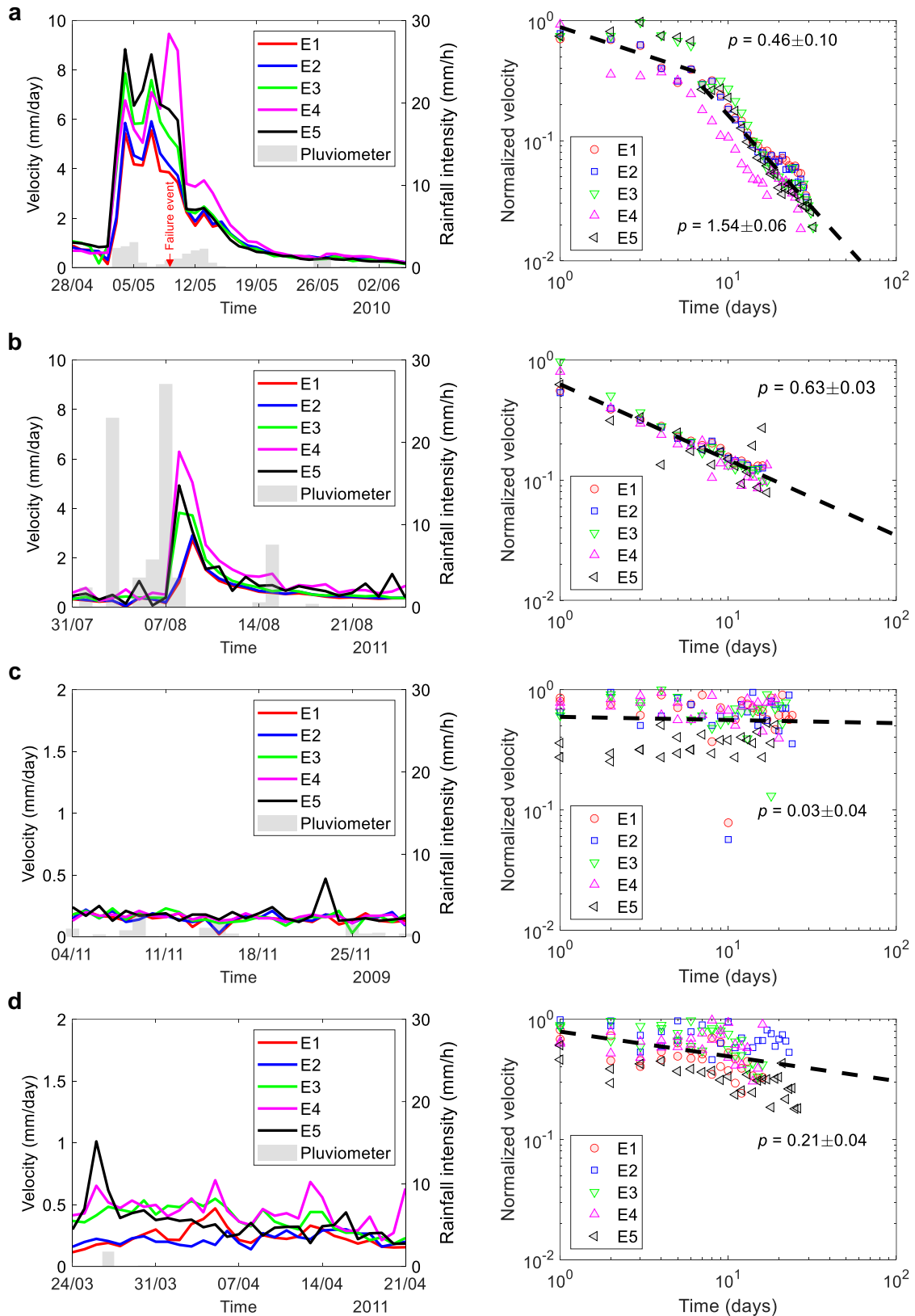


Fig. 3 Slope velocity time series measured by the five extensometers E1-E5 as well as rainfall intensity data recorded by the pluviometer (left panel) and post-peak velocity relaxation (right panel) for different types of peaks. **a** Type I, exogenous-subcritical; **b** Type II, exogenous-critical; **c** Type III, endogenous-subcritical; and **d** Type IV, endogenous-critical. The red arrow in **a** marks the timing of the local failure of a northern sector of the slope on 9 May 2010. In **c** and **d** right, pre-peak data are also indicated (open markers) in addition to post-peak data (filled markers).

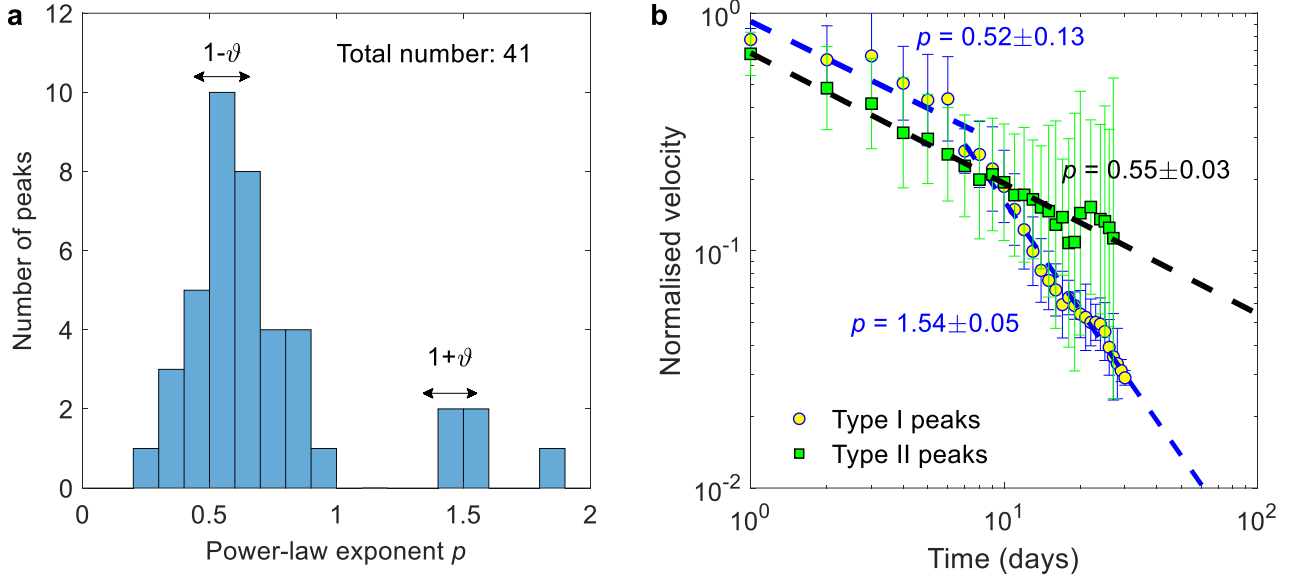


Fig. 4 Post-peak relaxation properties associated with detected peaks in the velocity time series. **a** Histogram of power law exponents p for post-peak velocity relaxation; the double arrows indicate the value ranges of $p = 1 - \vartheta$ (Type I peaks) and $p = 1 + \vartheta$ (Type II peaks), with $\vartheta \approx 0.45 \pm 0.1$. **b** Ensemble averaged velocity relaxation behavior for Type I and II peaks; error bars indicate the standard deviation associated with the ensemble average.

Discussion

We have presented a novel endo-exo theoretical framework to quantitatively classify episodic landslide movements into four fundamental types of distinct precursory/recovery signatures but related by a single common parameter ϑ . All the four types of landslide dynamics have been observed in the Preonzo landslide with $\vartheta \approx 0.45 \pm 0.10$, which is different from the mean-field solution $\vartheta \approx 0$ for creep ruptures in heterogeneous materials^{29–31}. Such a non-mean-field response reflects the intrinsic fluctuations and correlations resulting from triggered cascades of geomaterial mass motions in the landslide. This ϑ value close to 0.5 may be explained by the first-passage problem of an underlying random walk^{32,33}, where a daughter mass surrounding a mobilized mother mass is only triggered to move when the fluctuating stress first reaches the strength level for sliding or fracturing.

Our findings indicate that, in the Preonzo landslide, numerous velocity peaks induced by rainfall are characterized as exogenous-critical. This suggests that the landslide’s behavior in reaction to external disturbances is primarily driven by cascading events across multiple generations of mass movement triggers. Consequently, the collective response of the mass as a whole is slower and more sustained, controlled by a “dressed” memory kernel with an exponent $1 - \vartheta$, compared to the quicker individual mass responses, which are directed by a “bare” memory kernel with an exponent of $1 + \vartheta$. This implies that this landslide is operating around a critical state with the branching ratio n intermittently increasing and receding close to 1, likely due to the competing damage and healing processes. This physical picture refines the concept of self-organized criticality stating that many crustal phenomena like earthquakes and landslides are evolving in a statistically stationary state of marginal stability^{22,34–37}. This paradigm elucidates why certain rainfall events trigger episodic landslide movements while others do not, as illustrated in Fig. 3. This behavior stems from the system’s dynamic evolution, which, after each peak, settles into a state slightly

removed from, but not far from, criticality. Gradually, the system is pushed back towards the critical state by a continuous flow of external disturbances, such as rainfall, snowmelt, and diurnal temperature/humidity cycles⁵. In addition, we have documented a unique exogenous-subcritical type of episodic landslide dynamics, which is related to the local failure of a downslope sector of the slope²⁷ on 9 May 2010. Before showing a rapid exogenous-subcritical relaxation characterized by the large exponent $1 + \vartheta$, the landslide has actually experienced ~ 8 days of relatively slower exogenous-critical relaxation with the small exponent $1 - \vartheta$ (see Figs. 2a and 3a). Substituting this characteristic time $t^* \approx 8$ days together with $\vartheta \approx 0.45$ into equation (4) and the estimate $c \approx 1$ day, we obtain $n \approx 0.63$. This comparatively low branching ratio n is consistent with the fact that this local failure-induced shock did not lead to a system-sized collapse since only a few generations of failure cascades have developed. In contrast, the high n value observed in rainfall-induced exogenous-critical shocks could stem from rainwater infiltration’s tendency to impact the entire slope, resulting in more pronounced spreading behavior. In our dataset, we also observe the presence of endogenous-critical landslide dynamics, indicating that cascading mass movements play a dominant role in triggering landslides through a kind of self-organized criticality. However, they are usually associated with small-magnitude peaks and weak time-dependence (governed by a relaxation exponent of $1 - 2\vartheta$ close to 0), making them sometimes difficult to be discriminated from the endogenous-subcritical dynamics driven by random fluctuations.

Up to now, we have mainly focused on the “endo-exo” regime where the landslide evolution is characterized by numerous accelerating-decelerating creep episodes driven by the interplay of exogenous perturbation and endogenous maturation. As the mass of the landslide progressively weakens, it could transition into the supercritical regime^{21,22} with $n > 1$, where the number of triggering events in the system grows on average exponentially with time²³ or even faster²⁴. This critical transition is found to be often endogenously driven in different natural and social systems²⁰, which rationalizes why many rainfall-induced landslides catastrophically fail in the absence of exceptional precipitation events³⁸. If the supercritical regime is dominated by positive feedbacks with the slope acceleration behavior $\dot{v}(t) \propto v(t)^m$ characterized by $m > 1$, the system will exhibit a finite-time singularity and thus a catastrophic failure³⁹⁻⁴¹.

We fit the velocity time series of the Preonzo landslide prior to its major collapse on 15 May 2012 (Fig. 5a) to a finite-time singularity power law (3) with exponent $p = 1/(m - 1)$. We find it necessary to consider two power law branches, one with $p \approx 1.88$ ($m \approx 1.53$) for the early stage and the second one with $p \approx 0.49$ ($m \approx 3.04$) for the final stage (Fig. 5b). This suggests that the system is indeed dominated by positive feedbacks which seem to strengthen close to the final collapse. Our previous work showed that these late stage large velocities are “dragon-kings”⁴² — a double metaphor for an event of a predominant impact/size like a “king” and a unique origin like a “dragon”⁴³. This break in power law scaling thus marks the transition of the system from the self-organized criticality regime where a catastrophic failure is unpredictable (the so-called “black-swan” regime)⁴⁴ to the dragon-king regime where a catastrophic failure becomes predictable⁴³. Such a two-branch time-to-failure power law behavior has also been observed in the ground deformational response prior to the volcanic eruption at Mount St Helens⁴⁵. Interestingly, when the Preonzo landslide entered the dragon-king regime, it once experienced a temporary deceleration during 7-11 May 2012 just before the final collapse. Such a precursory quiescence is consistent with the theoretical prediction for the supercritical regime²³ with $n > 1$ and $\vartheta > 0$. Substituting $t^* \approx 4$ days and $\vartheta \approx 0.45$ into equation (4) which also holds for the supercritical regime²³, we obtain

$n \approx 7.5$, indicating an intense explosive branching process. Similar precursory quiescence phenomena have been observed prior to great earthquakes⁴⁶ and volcanic eruptions⁴⁷.

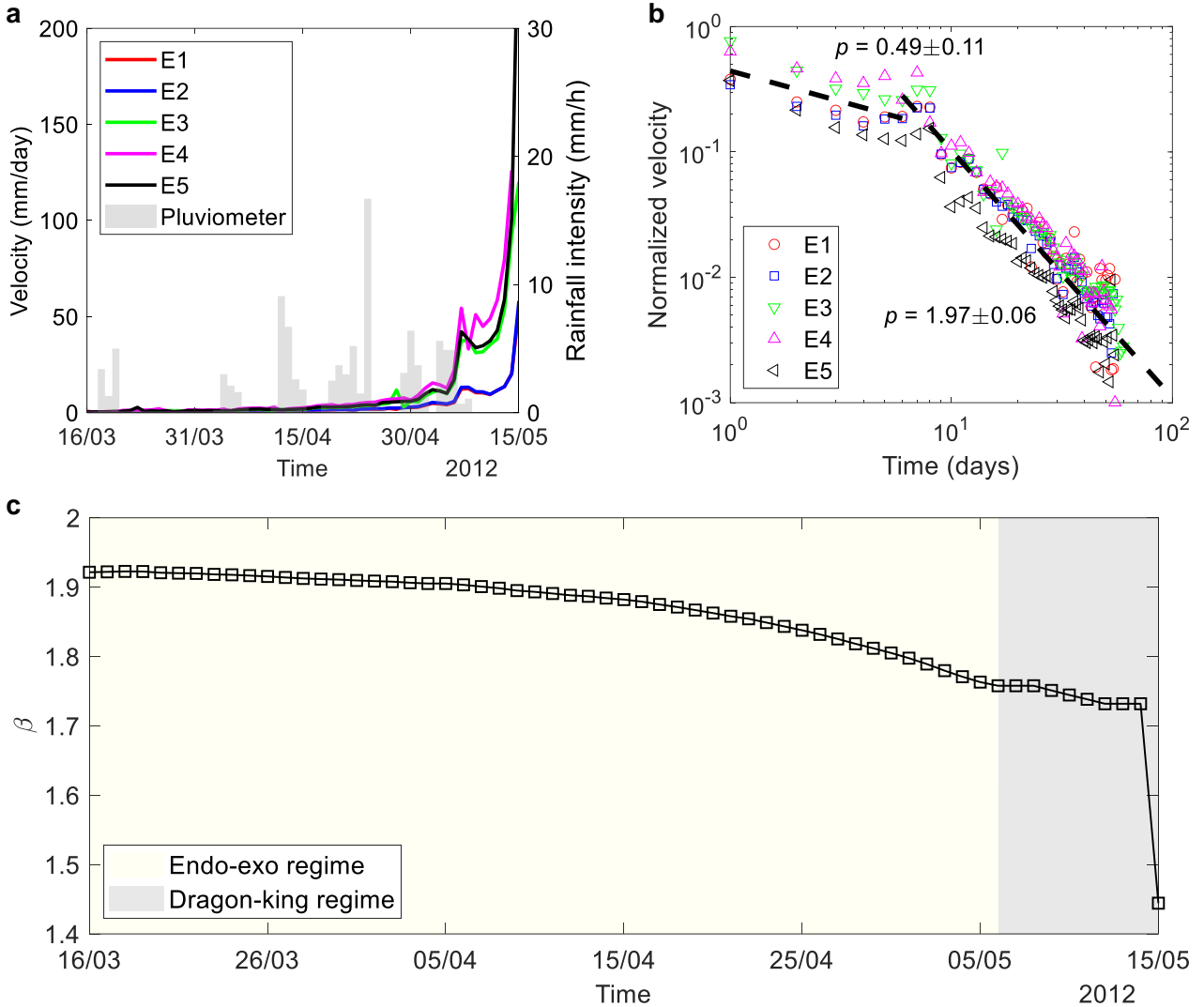


Fig. 5 Evolution of the Preonzo landslide prior to its major collapse on 15 May 2012. **a** Time series of the slope velocity measured by the five extensometers E1-E5 as well as rainfall intensity data recorded by the pluviometer. **b** Variation of normalized velocity prior to the catastrophic failure as a function of time to the failure (time flows from right to left), which is fitted to a two-branch finite-time singularity power law (indicated by the dashed line). **c** Progressive decline of the β -value of the velocity probability distribution, indicating a transition of the landslide from an endo-exo (subcritical/critical) regime characterized by episodic movements to a dragon-king (supercritical) regime ending with a catastrophic failure.

Drawing parallels between landslides and earthquakes^{8,11,48-51}, we postulate that the condition for this subcritical/critical-to-supercritical transition to occur²⁴ is that the system shifts from $\alpha < \mu$ to $\alpha \geq \mu$, where α is the exponent in the productivity law $\rho(E) \propto E^\alpha$ defining the number of daughter masses triggered by a mother mass of energy release E , while μ is the exponent in the Gutenberg-Richter-type probability density distribution of daily energy release of the landslide $f(E(t)) \propto E(t)^{-(1+\mu)}$. Given $E(t) \propto v(t)^2$, we derive $f(v(t)) \propto v(t)^{-(1+2\mu)}$ from the law of conservation of probability under a change of variable²². Our previous work suggests that the probability distribution of the $v(t)$'s of the Preonzo landslide follows an inverse gamma

distribution (with β denoting its shape parameter; see Methods) characterized by a power law tail⁵² $f(v(t)) \propto v(t)^{-(1+\beta)}$, with therefore $\beta = 2\mu$. It is found that β progressively drops from 1.92 to 1.76 (correspondingly, μ drops from 0.96 to 0.88) over 1-2 months (Fig. 5c). This indicates a higher occurrence rate of moderate to large velocities as the slope approaches the critical transition from the endo-exo regime (dominated by small velocities) to the dragon-king regime (dominated by large velocities) at ~ 1 week before the final collapse⁴². Thus, we would expect $\alpha \approx 0.88$, which is comparable to the typical value of $\alpha \approx 0.8$ for earthquakes⁵³. This correspondence holds notwithstanding the fact that landslides happen in near-surface environments under low stress conditions, while earthquakes occur in deep subsurface regions subject to much higher stress levels. The decrease of β (and μ) prior to catastrophic landslides is similar to the observed b -value decline prior to great earthquakes⁵⁴⁻⁵⁶, which is possibly due to increased differential stresses on rock bridges/asperities accommodating crack propagations⁵⁷ and/or enhanced differential stresses on creeping fault patches promoting slip ruptures⁵⁸. It also finds a natural explanation in the context of cascading triggered events described by self-excited conditional point processes⁵⁹. This observation points to the possibility to predict catastrophic landslides by monitoring the temporal evolution of the β -value. These results demonstrating parallels between landslides and earthquakes provide additional supports for the fault mechanics perspective of landslide dynamics and failure^{8,11,48-51}.

Our novel conceptual framework points at the existence of a deep quantitative relationship between episodic landslide movements, external triggering events (e.g., rainfall, snowmelt, and seismicity), and internal frictional slip, damage, and healing processes within the landmass. The results and insights obtained in the current work are of significant value for landslide hazard prediction and mitigation, from both the conceptual and operational points of view. Based on the well-documented dataset of the Preonzo landslide, we have provided a thorough validation of this framework, which can be applied to many other landslides showing similar episodic movements⁴⁻¹². We will report the application of our endo-exo framework to additional landslide cases in subsequent publications. The endo-exo framework established in our work has far-reaching implications for predicting and mitigating various geohazards, including not only landslides, but also earthquakes, rockbursts, volcanic eruptions, and glacier breakoffs, which all exhibit similar episodic deformations and sometimes also show transitions into catastrophic failures.

Methods

Mean field solution of the model of self-excited triggered mass movements. Considering the exogenous source $V(t)$ given by a delta function $\delta(t)$ centered at the origin of time, we obtain the Green function of equation (2), also called a dressed or renormalized memory kernel $\Psi(t - \tau)$, which is the solution of^{16,23}:

$$\Psi(t) = \delta(t) + n \int_{-\infty}^t \psi(t - \tau) \Psi(\tau) d\tau, \quad (5)$$

such that:

$$v(t) = \int_{-\infty}^t V(\tau) \Psi(t - \tau) d\tau, \quad (6)$$

which is the solution of equation (2). Here, equation (6) expresses the fact that the present velocity $v(t)$ results from all past exogenous sources $V(\tau)$ mediated to the present by the dressed memory

kernel $\Psi(t - \tau)$ incorporating all the generations of cascades of influences²⁰. For the case where the bare propagator is given by equation (1), the recovery dynamics of the system after a strong external event $V(\tau) \propto \delta(\tau - t_c)$ is fully controlled by the dressed memory kernel¹⁶, such that:

$$v(t) = \Psi(t) \propto \begin{cases} 1/(t - t_c)^{1-\vartheta}, & \text{for } c < t - t_c < t^*, \\ 1/(t - t_c)^{1+\vartheta}, & \text{for } t - t_c > t^*, \end{cases} \quad (7)$$

where t_c is the critical time chosen as the time of the peak and t^* is the characteristic time given by equation (4).

In the absence of strong external events, a peak in landslide velocity can also spontaneously occur due to the interplay of a continuous stochastic flow of small external perturbations and the amplifying impact of the epidemic cascade of endogenous interactions. The average velocity trajectory before and after the peak, conditioned on the existence of a peak, is given by $\langle v(t) | v(t_c) \rangle \propto \text{Cov}(v(t), v(t_c))$, so the precursory and recovery dynamics associated with the peak are governed by¹⁶:

$$v(t) \propto \int_{-\infty}^{t-t_c} \Psi(t - t_c - \tau) \Psi(-\tau) d\tau \propto 1/|t - t_c|^{1-2\vartheta}, \text{ for } c < |t - t_c| < t^*, \quad (8)$$

or equivalently for $n \rightarrow 1$ (critical regime). If $n < 1$ (subcritical regime), the system response is essentially a noise process largely driven by random fluctuations, described by²⁵:

$$v(t) \propto 1/|t - t_c|^0, \text{ for } |t - t_c| > t^*. \quad (9)$$

Calculation of normalized velocities around a peak. We compute normalized slope velocities $\tilde{v}(t)$ around a peak based on the following equation:

$$\tilde{v}(t) = (v(t) - v_0)/(v(t_c) - v_0), \quad (10)$$

where the slope velocity $v(t)$ reaches a peak value of $v(t_c)$ at time $t = t_c$ and v_0 is the residual velocity when the landslide system has fully recovered from external perturbations. However, the determination of this residual velocity for a rainfall-induced landslide (like the Preonzo landslide) is subject to significant uncertainties, because the landslide has very rare opportunities to completely recover from one rainfall event before the next one occurs. In this work, we estimate the residual velocity by first detecting troughs in the velocity time series. We qualify a trough in the velocity time series as a local minimum over a 20-day time window which is at least $k = 2.5$ times smaller than the 2-month average velocity. The time window sizes and the threshold value k are chosen to give an effective and reasonable detection of peaks and troughs from the data (see Supplementary Fig. 2), but the results do not significantly change by varying these parameters (see Supplementary Figs. 7-10 and 13). We then define the residual velocity associated with a given peak as the minimum of the two nearest troughs (with one before the peak and one after the peak). Note that this residual velocity tends to vary over time reflecting the nonstationary characteristic of the landslide. Supplementary Fig. 11 shows the probability density function of calculated residual velocities (associated with the identified peaks in Supplementary Fig. 6), which have a mean of 0.008 mm/day. We have also tested other possible approaches of determining the residual velocity, e.g., based on the average of the 10 nearest troughs around a peak or based on the minimum/average of the troughs located between the former peak and the latter peak. No significant changes in the results are found.

Power law calibration of velocity time series around a peak. We fit the time series of normalized velocities $\tilde{v}(t)$ around a peak to the finite-time singularity power law function:

$$\tilde{v}(t) = A/|t - t_c|^p, \quad (11)$$

where t_c is the critical time chosen as the time of the peak, A is a constant, and p is the power law exponent. To estimate A and p , we use the method of least squares to minimize the sum of squared residuals

$$s = \sum_{t_i} r(t_i)^2, \quad (12)$$

with each residual calculated as

$$r(t_i) = \log \tilde{v}(t_i) - \log A + p \log |t_i - t_c|. \quad (13)$$

We then set the partial derivatives $\partial s / \partial (\log A)$ and $\partial s / \partial p$ to be both zero, leading to solve a linear system of two equations with the two unknowns A and p .

Inverse gamma distribution. The probability density function of the three-parameter inverse gamma distribution is written as^{42,60}:

$$f(v) = \frac{\alpha^\beta}{\Gamma(\beta)} \left(\frac{1}{v-\gamma} \right)^{\beta+1} \exp\left(-\frac{\alpha}{v-\gamma}\right), \quad (14)$$

where v is the slope velocity, α is a scale parameter, β is a shape parameter equal to the exponent of the asymptotic power law tail for large v 's (according to the mathematical convention in the theory of Lévy stable laws²²), γ is a threshold velocity, and $\Gamma(\cdot)$ is the gamma function. The parameters need to meet the conditions of $\alpha > 0$, $\beta > 0$, and $\gamma < v$. The parameters α , β , and γ can be determined based on the profile maximum likelihood estimation method³⁹. The inverse gamma distribution has an essential singularity at $v = \gamma$ and the corresponding rollover for v 's around the mode $\alpha / (\beta + 1) + \gamma$, and a power law decay with a tail exponent β for medium and large v values, so that the tail of the inverse gamma tends to converge to the power law⁵²

$$f(v) \approx \frac{\alpha^\beta}{\Gamma(\beta)} v^{-\beta-1}, \text{ for } v \gg \alpha + \gamma. \quad (15)$$

Data availability

The slope displacement monitoring data of the Preonzo landslide are publicly available at the ETH Zurich Research Collection (<https://doi.org/10.3929/ethz-b-000600495>).

References

1. Petley, D. N. Global patterns of loss of life from landslides. *Geology* **40**, 927–930 (2012).
2. Palmer, J. Creeping earth could hold secret to deadly landslides. *Nature* **548**, 384–386 (2017).
3. Gariano, S. L. & Guzzetti, F. Landslides in a changing climate. *Earth Sci Rev* **162**, 227–252 (2016).
4. Agliardi, F., Scuderi, M. M., Fusi, N. & Collettini, C. Slow-to-fast transition of giant creeping rockslides modulated by undrained loading in basal shear zones. *Nat Commun* **11**, 1–11 (2020).
5. Bontemps, N., Lacroix, P., Larose, E., Jara, J. & Taïpe, E. Rain and small earthquakes maintain a slow-moving landslide in a persistent critical state. *Nat Commun* **11**, 1–10 (2020).
6. Crosta, G. B. *et al.* Chasing a complete understanding of the triggering mechanisms of a large rapidly evolving rockslide. *Landslides* **11**, 747–764 (2014).
7. Crosta, G. B., Agliardi, F., Rivolta, C., Alberti, S. & Dei Cas, L. Long-term evolution and early warning strategies for complex rockslides by real-time monitoring. *Landslides* **14**, 1615–1632 (2017).
8. Finnegan, N. J., Brodsky, E. E., Savage, H. M., Nereson, A. L. & Murphy, C. R. Seasonal slow landslide displacement is accommodated by mm-scale stick-slip events. *Geophys Res Lett* **49**, e2022GL099548 (2022).
9. Handwerger, A. L., Roering, J. J. & Schmidt, D. A. Controls on the seasonal deformation of

- slow-moving landslides. *Earth Planet Sci Lett* **377–378**, 239–247 (2013).
10. Hu, X., Bürgmann, R., Schulz, W. H. & Fielding, E. J. Four-dimensional surface motions of the Slumgullion landslide and quantification of hydrometeorological forcing. *Nat Commun* **11**, 1–9 (2020).
 11. Lacroix, P., Perfettini, H., Taïpe, E. & Guillier, B. Coseismic and postseismic motion of a landslide: Observations, modeling, and analogy with tectonic faults. *Geophys Res Lett* **41**, 6676–6680 (2014).
 12. Finnegan, N. J., Perkins, J. P., Nereson, A. L. & Handwerger, A. L. Unsaturated Flow Processes and the Onset of Seasonal Deformation in Slow-Moving Landslides. *J Geophys Res Earth Surf* **126**, (2021).
 13. Lacroix, P., Handwerger, A. L. & Bièvre, G. Life and death of slow-moving landslides. *Nat Rev Earth Environ* **1**, 404–419 (2020).
 14. Scholz, C. H. *The Mechanics of Earthquakes and Faulting*. (Cambridge University Press, Cambridge, 2019). doi:10.1017/9781316681473.
 15. Saichev, A. & Sornette, D. Generation-by-generation dissection of the response function in long memory epidemic processes. *Eur Phys J B* **75**, 343–355 (2010).
 16. Sornette, D. & Helmstetter, A. Endogenous versus exogenous shocks in systems with memory. *Physica A: Statistical Mechanics and its Applications* **318**, 577–591 (2003).
 17. Andrade, E. N. D. C. On the viscous flow in metals, and allied phenomena. *Proceedings of the Royal Society of London A* **84**, 1–12 (1910).
 18. Utsu, T., Ogata, Y. & Ritsuko, S. M. The centenary of the Omori formula for a decay law of aftershock activity. *Journal of Physics of the Earth* **43**, 1–33 (1995).
 19. Hawkes, A. G. & Oakes, D. A cluster process representation of a self-exciting process. *J Appl Probab* **11**, 493–503 (1974).
 20. Sornette, D. Endogenous versus Exogenous Origins of Crises. in *Extreme Events in Nature and Society* (eds. Albeverio, S., Jentsch, V. & Kantz, H.) 95–119 (Springer, Heidelberg, 2006). doi:10.1007/3-540-28611-X_5.
 21. Harris, T. E. *The Theory of Branching Processes*. (Springer, Berlin, 1963).
 22. Sornette, D. *Critical Phenomena in Natural Sciences - Chaos, Fractals, Selforganization and Disorder: Concepts and Tools*. (Springer, Berlin, 2006).
 23. Helmstetter, A. & Sornette, D. Subcritical and supercritical regimes in epidemic models of earthquake aftershocks. *J Geophys Res Solid Earth* **107**, ESE 10-1-ESE 10-21 (2002).
 24. Sornette, D. & Helmstetter, A. Occurrence of finite-time singularities in epidemic models of rupture, earthquakes, and starquakes. *Phys Rev Lett* **89**, 158501 (2002).
 25. Crane, R. & Sornette, D. Robust dynamic classes revealed by measuring the response function of a social system. *Proc Natl Acad Sci U S A* **105**, 15649–15653 (2008).
 26. Sornette, D., Deschâtres, F., Gilbert, T. & Ageon, Y. Endogenous versus exogenous shocks in complex networks: An empirical test using book sale rankings. *Phys Rev Lett* **93**, 1–4 (2004).
 27. Loew, S., Gschwind, S., Gischig, V., Keller-Signer, A. & Valenti, G. Monitoring and early warning of the 2012 Preonzo catastrophic rock slope failure. *Landslides* **14**, 141–154 (2017).
 28. Gschwind, S., Loew, S. & Wolter, A. Multi-stage structural and kinematic analysis of a retrogressive rock slope instability complex (Preonzo, Switzerland). *Eng Geol* **252**, 27–42 (2019).
 29. Nechad, H., Helmstetter, A., El Guerjouma, R. & Sornette, D. Andrade and critical time-to-

- failure laws in fiber-matrix composites: Experiments and model. *J Mech Phys Solids* **53**, 1099–1127 (2005).
30. Nechad, H., Helmstetter, A., El Guerjouma, R. & Sornette, D. Creep ruptures in heterogeneous materials. *Phys Rev Lett* **94**, 045501 (2005).
 31. Saichev, A. & Sornette, D. Andrade, Omori, and time-to-failure laws from thermal noise in material rupture. *Phys Rev E* **71**, 016608 (2005).
 32. Redner, S. *A Guide to First-Passage Processes*. (Cambridge University Press, Cambridge, 2001). doi:10.1017/CBO9780511606014.
 33. Saichev, A. & Sornette, D. Effects of diversity and procrastination in priority queuing theory: The different power law regimes. *Phys Rev E Stat Nonlin Soft Matter Phys* **81**, 1–13 (2010).
 34. Bak, P. & Tang, C. Earthquakes as a self-organized critical phenomenon. *J Geophys Res Solid Earth* **94**, 15635–15637 (1989).
 35. Main, I. Statistical physics, seismogenesis, and seismic hazard. *Reviews of Geophysics* **34**, 433–462 (1996).
 36. Sornette, A. & Sornette, D. Self-organized criticality and earthquakes. *Europhys Lett* **9**, 197–202 (1989).
 37. Turcotte, D. L. Self-organized criticality. *Reports on Progress in Physics* **62**, 1377–1429 (1999).
 38. Eberhardt, E. Twenty-ninth Canadian Geotechnical Colloquium: The role of advanced numerical methods and geotechnical field measurements in understanding complex deep-seated rock slope failure mechanisms. *Canadian Geotechnical Journal* **45**, 484–510 (2008).
 39. Lei, Q., Sornette, D., Yang, H. & Loew, S. Real-time forecast of catastrophic landslides via dragon-king detection. *Geophys Res Lett* **50**, e2022GL100832 (2023).
 40. Lei, Q. & Sornette, D. A stochastic dynamical model of slope creep and failure. *Geophys Res Lett* **50**, e2022GL102587 (2023).
 41. Sornette, D. Predictability of catastrophic events: Material rupture, earthquakes, turbulence, financial crashes, and human birth. *Proc Natl Acad Sci U S A* **99**, 2522–2529 (2002).
 42. Lei, Q., Sornette, D., Yang, H. & Loew, S. Real-time forecast of catastrophic landslides via dragon-king detection. *Geophys Res Lett* **50**, e2022GL100832 (2023).
 43. Sornette, D. & Ouillon, G. Dragon-kings: Mechanisms, statistical methods and empirical evidence. *European Physical Journal: Special Topics* **205**, 1–26 (2012).
 44. Taleb, N. N. *The Black Swan: The Impact of the Highly Improbable*. (Penguin, London, 2010).
 45. Voight, B. A method for prediction of volcanic eruptions. *Nature* **332**, 125–130 (1988).
 46. Scholz, C. H. *The Mechanics of Earthquakes and Faulting*. (Cambridge University Press, Cambridge, 2019). doi:10.1017/9781316681473.
 47. Sigmundsson, F. *et al.* Deformation and seismicity decline before the 2021 Fagradalsfjall eruption. *Nature* **609**, 523–528 (2022).
 48. Gomberg, J., Bodin, P., Savage, W. & Jackson, M. E. Landslide faults and tectonic faults, analogs?: The Slumgullion earthflow, Colorado. *Geology* **23**, 41–44 (1995).
 49. Handwerger, A. L., Rempel, A. W., Skarbek, R. M., Roering, J. J. & Hilley, G. E. Rate-weakening friction characterizes both slow sliding and catastrophic failure of landslides. *Proc Natl Acad Sci U S A* **113**, 10281–10286 (2016).
 50. Helmstetter, A. *et al.* Slider block friction model for landslides: Application to Vaiont and La Clapière landslides. *J Geophys Res Solid Earth* **109**, 1–15 (2004).

51. Viesca, R. C. & Rice, J. R. Nucleation of slip-weakening rupture instability in landslides by localized increase of pore pressure. *J Geophys Res Solid Earth* **117**, 1–21 (2012).
52. Lei, Q. & Sornette, D. A stochastic dynamical model of slope creep and failure. *Geophys Res Lett* **50**, e2022GL102587 (2023).
53. Helmstetter, A. Is earthquake triggering driven by small earthquakes? *Phys Rev Lett* **91**, 3–6 (2003).
54. Smith, W. D. The b-value as an earthquake precursor. *Nature* **289**, 136–139 (1981).
55. Nakaya, S. Spatiotemporal variation in b value within the subducting slab prior to the 2003 Tokachi-oki earthquake (M 8.0), Japan. *J Geophys Res Solid Earth* **111**, 1–13 (2006).
56. Imoto, M. Changes in the magnitude-frequency b-value prior to large (M \geq 6.0) earthquakes in Japan. *Tectonophysics* **193**, 311–325 (1991).
57. Scholz, C. H. On the stress dependence of the earthquake b value. *Geophys Res Lett* **42**, 1399–1402 (2015).
58. Ito, R. & Kaneko, Y. Physical mechanism for a temporal decrease of the Gutenberg-Richter b -value prior to a large earthquake. *J Geophys Res Solid Earth* **128**, 1–21 (2023).
59. Helmstetter, A. & Sornette, D. Predictability in the Epidemic-Type Aftershock Sequence model of interacting triggered seismicity. *J Geophys Res Solid Earth* **108**, 2482 (2003).
60. Forbes, C., Evans, M., Hastings, N. & Peacock, B. *Statistical Distributions*. (John Wiley & Sons, New Jersey, 2011).

Acknowledgement

Q.L. is grateful for the support by the Swiss National Science Foundation (Grant No. 189882) and the National Natural Science Foundation of China (Grant No. 41961134032). D.S. acknowledges partial support from the National Natural Science Foundation of China (Grant No. U2039202, T2350710802), from the Shenzhen Science and Technology Innovation Commission (Grant No. GJHZ20210705141805017) and the Center for Computational Science and Engineering at the Southern University of Science and Technology.

Author contributions

Q.L. and D.S. designed the research; Q.L. conducted the research; Q.L. and D.S. analyzed the results; Q.L. wrote the manuscript; D.S. reviewed and edited the manuscript.

Competing interests

The authors declare no competing interests.

Additional information

Correspondence and requests for materials should be addressed to Q.L.

Supplementary Information for:
Exo-endo framework for a unifying classification
of episodic landslide movements

Qinghua Lei^{1,*}, Didier Sornette²

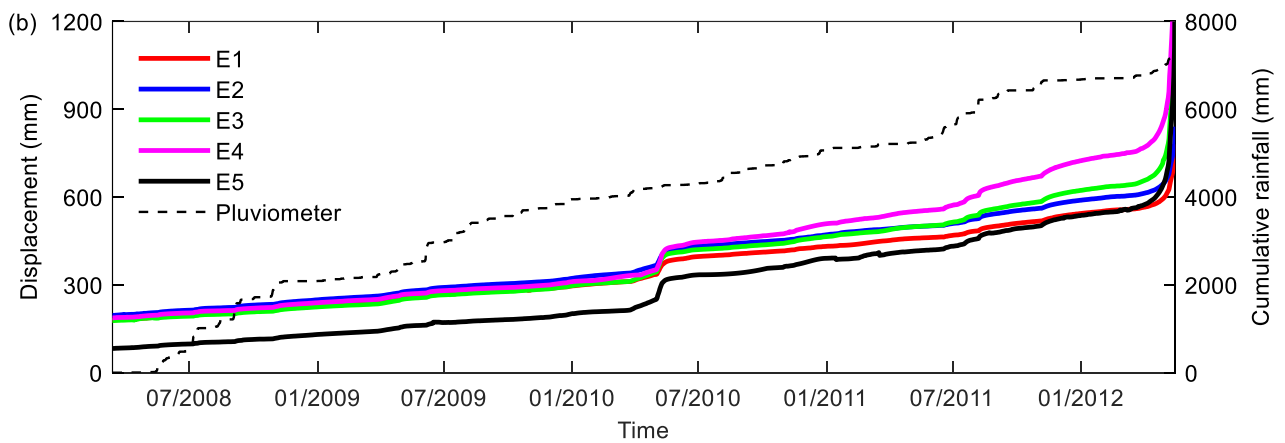
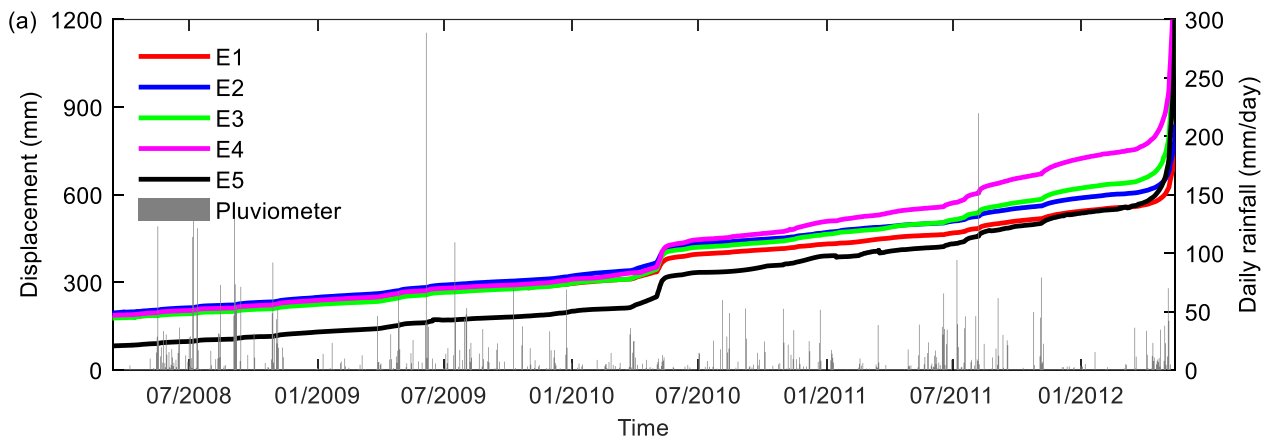
¹*Department of Earth Sciences, Uppsala University, Uppsala, Sweden*

²*Institute of Risk Analysis, Prediction and Management, Academy for Advanced Interdisciplinary Studies, Southern University of Science and Technology, Shenzhen, China*

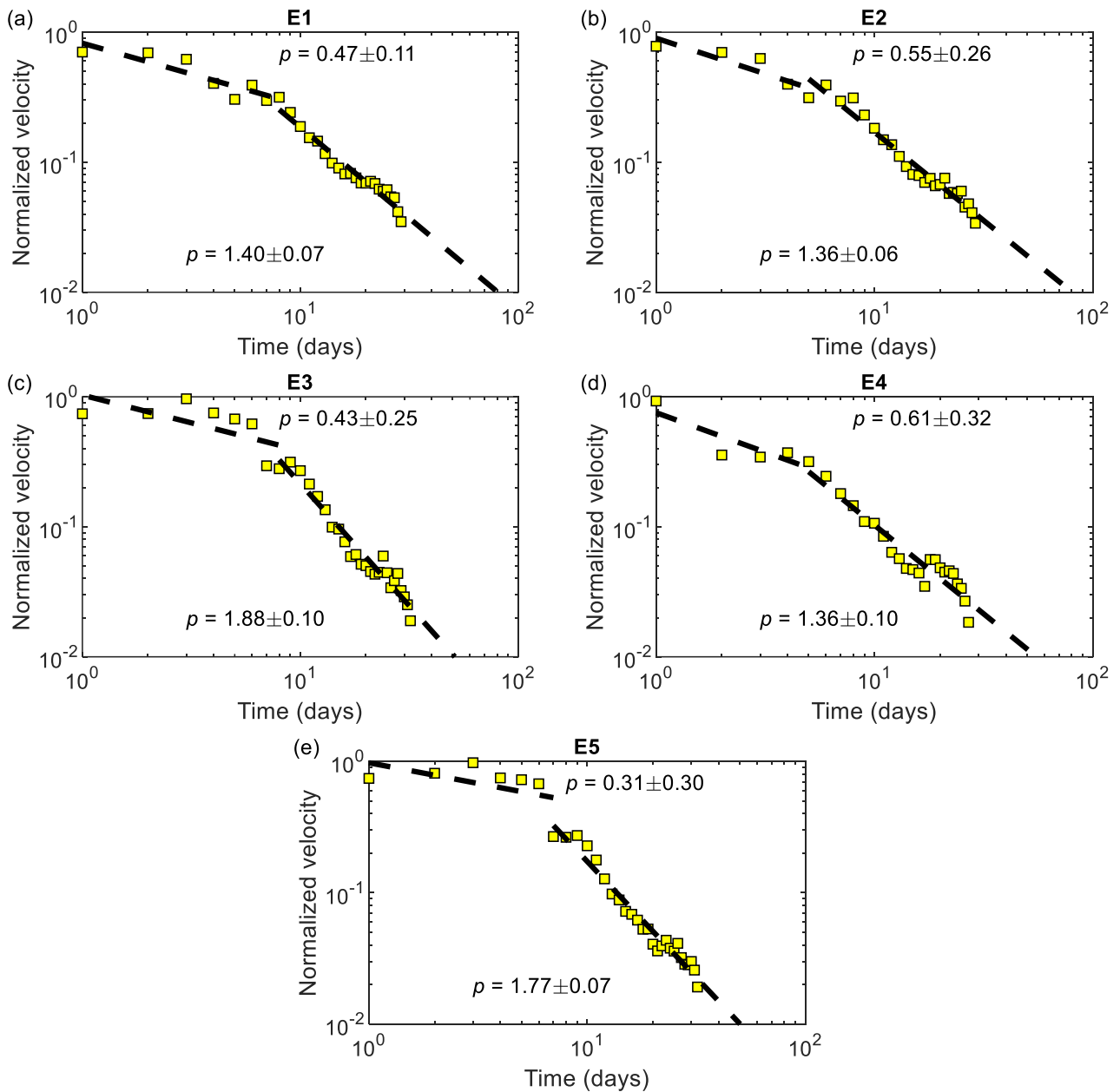
This document includes:

Supplementary Figs. 1-14.

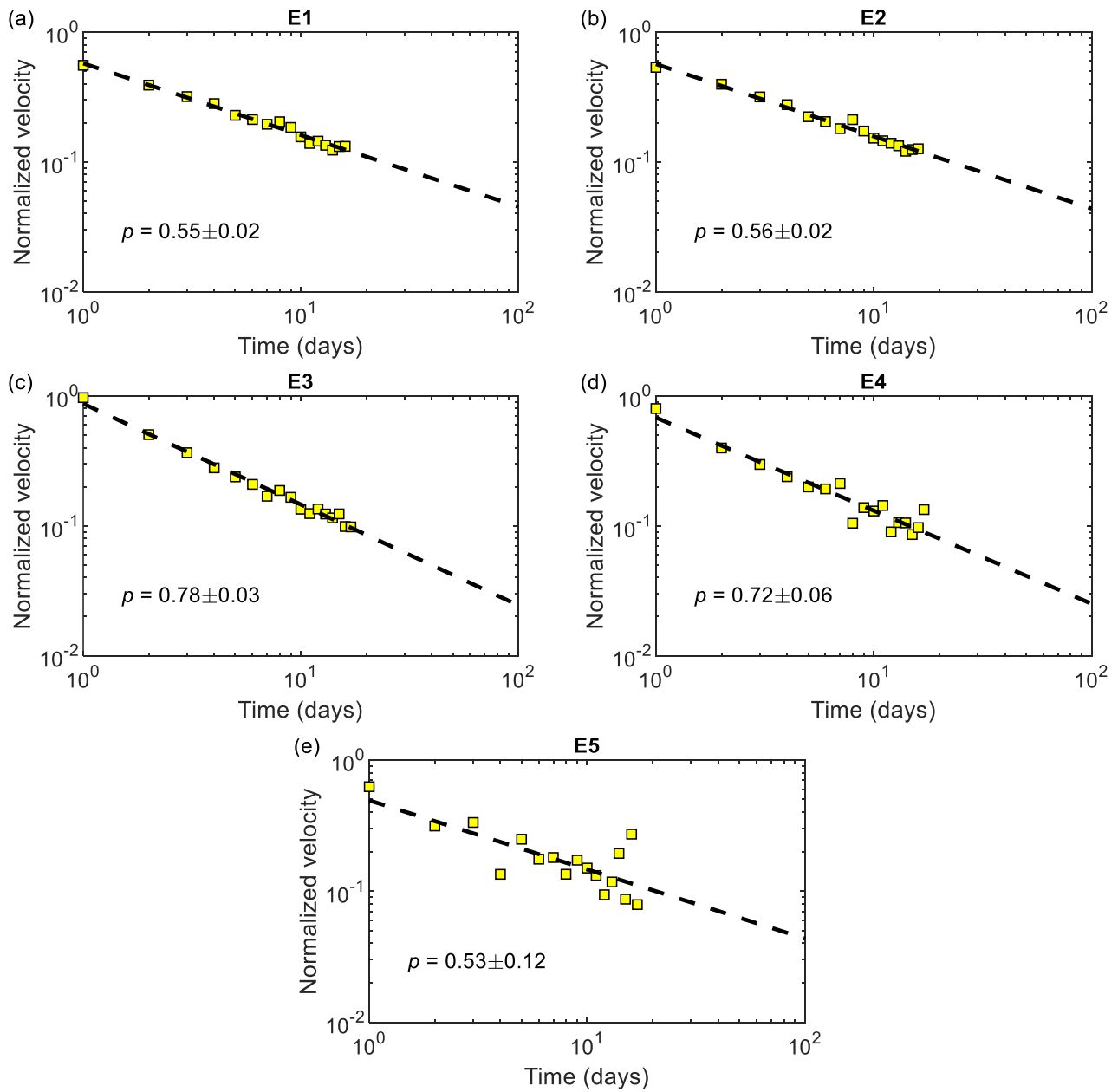
* Corresponding author: qinghua.lei@geo.uu.se



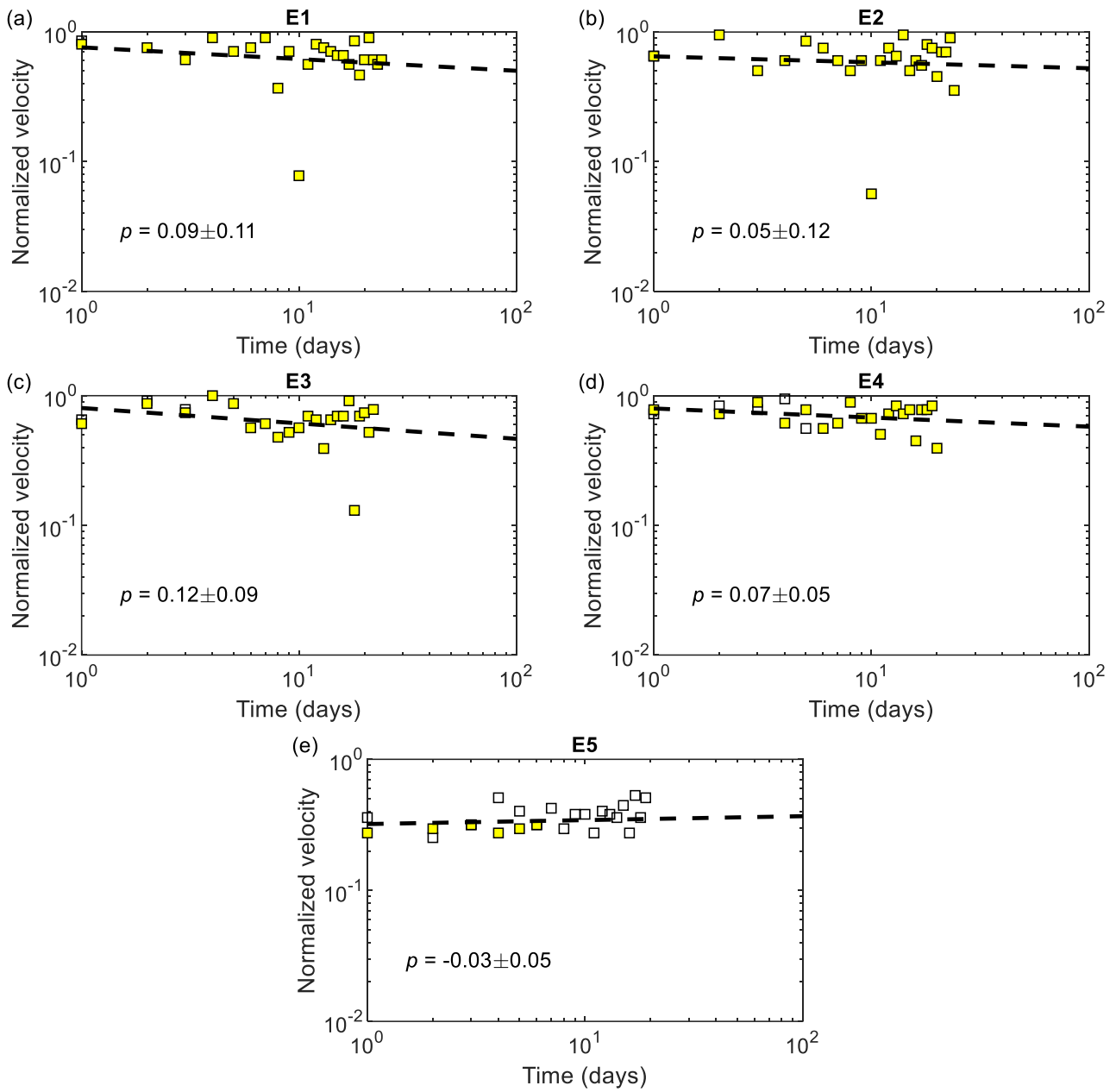
Supplementary Fig. 1 Monitoring data of the Preonzo landslide, Switzerland. Time series of slope displacements measured by five extensometers presented together with the data of **a** daily rainfall and **b** cumulative rainfall recorded by a pluviometer installed at the Preonzo slope.



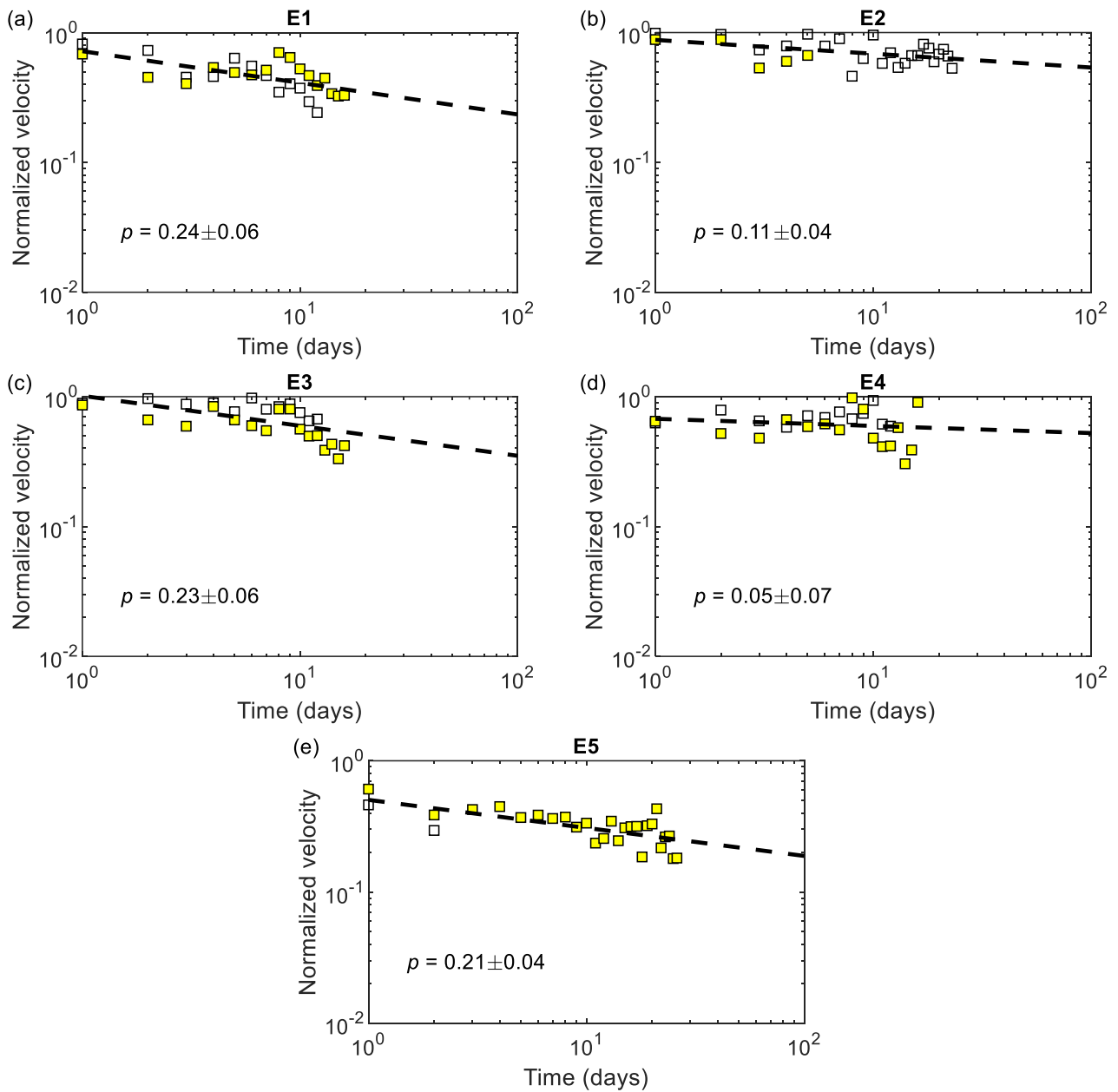
Supplementary Fig. 2 Post-peak relaxation of Type I exogenous-subcritical peaks. Variation of normalized velocity as a function of post-peak time for the five extensometers E1-E5.



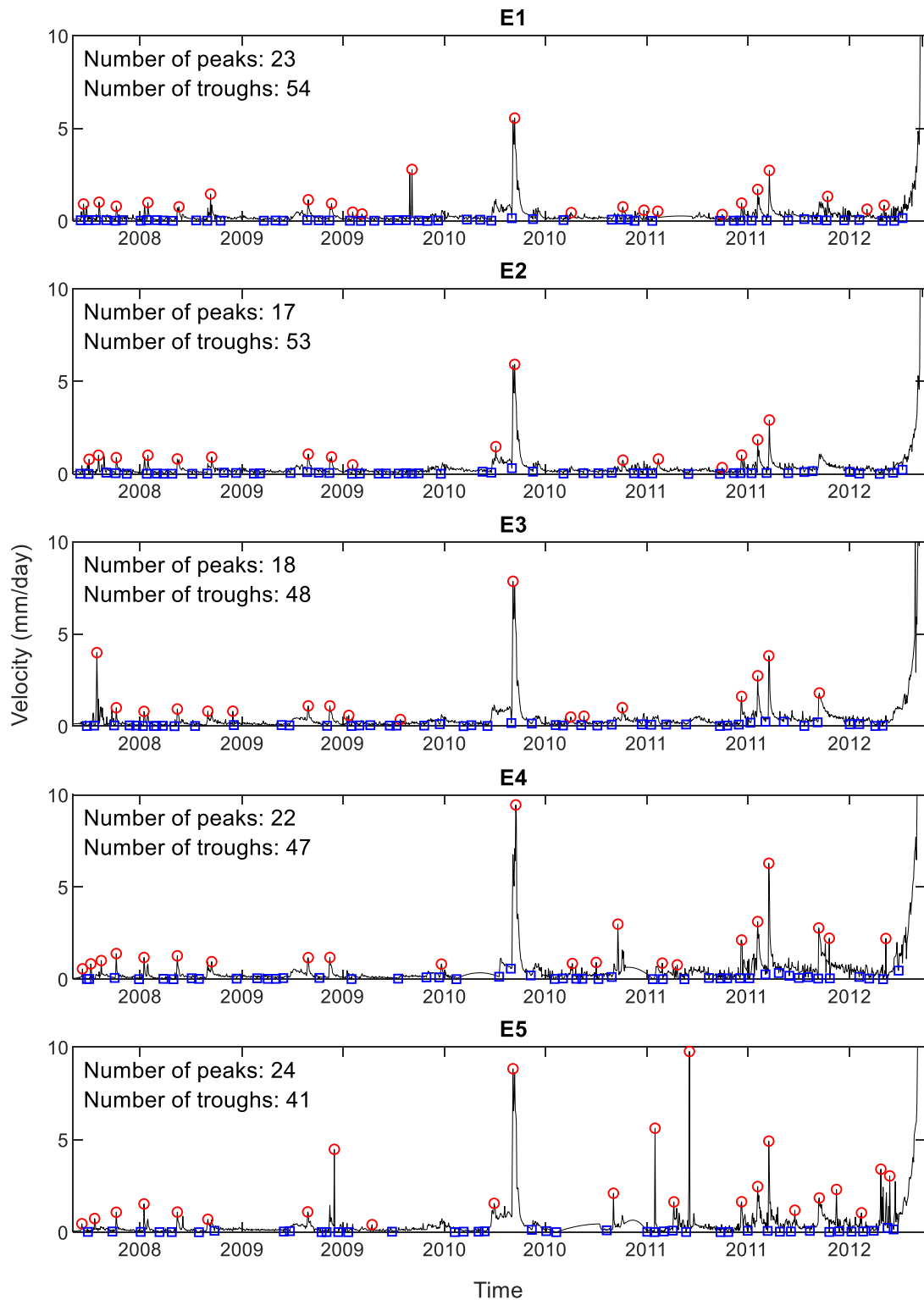
Supplementary Fig. 3 Post-peak relaxation of Type II exogenous-critical peaks. Variation of normalized velocity as a function of post-peak time for the five extensometers E1-E5.



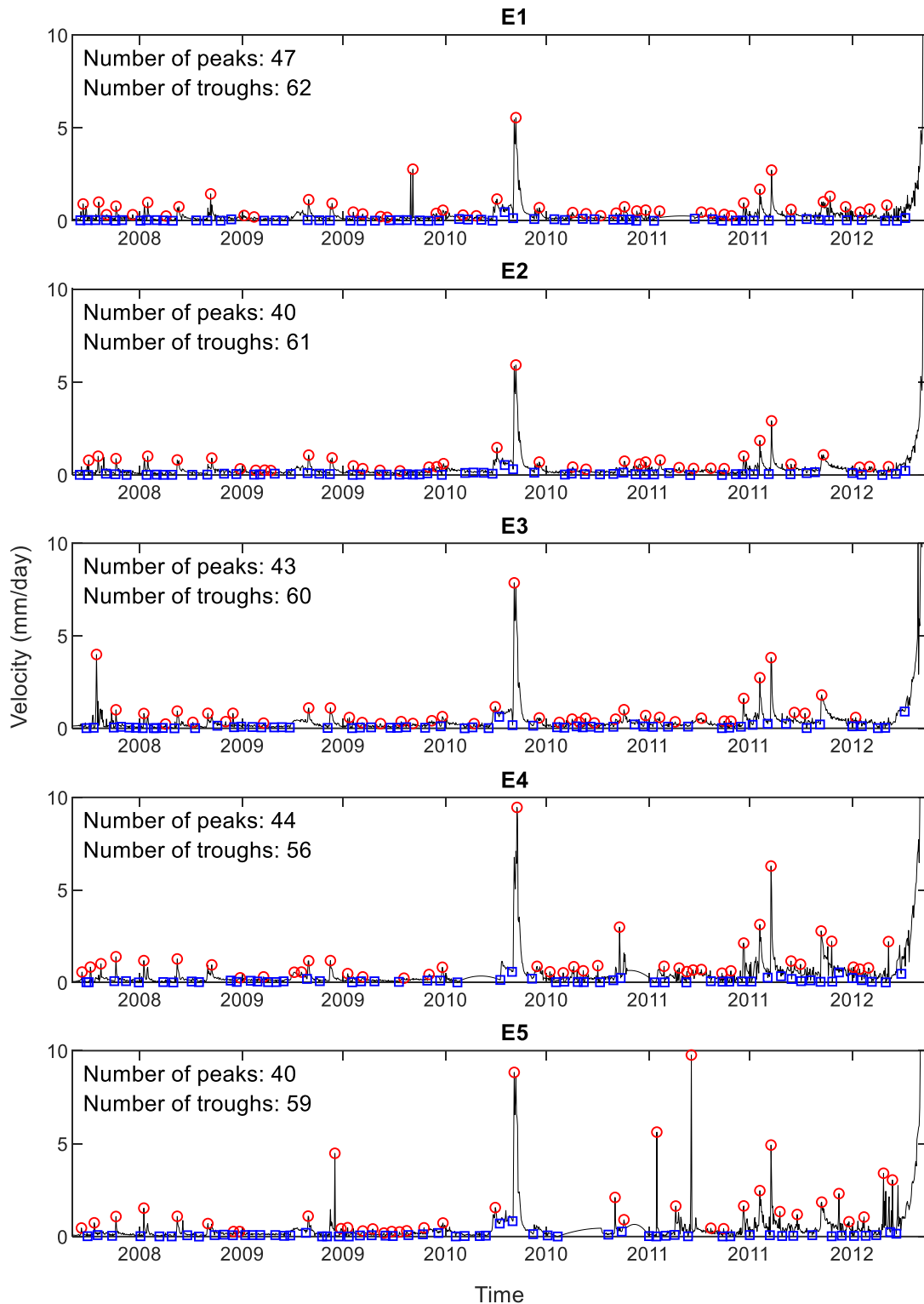
Supplementary Fig. 4 Pre-peak (open symbols) acceleration and post-peak (colored symbols) relaxation of Type III exogenous-subcritical peaks. Variation of normalized velocity as a function of pre/post-peak time for the five extensometers E1-E5.



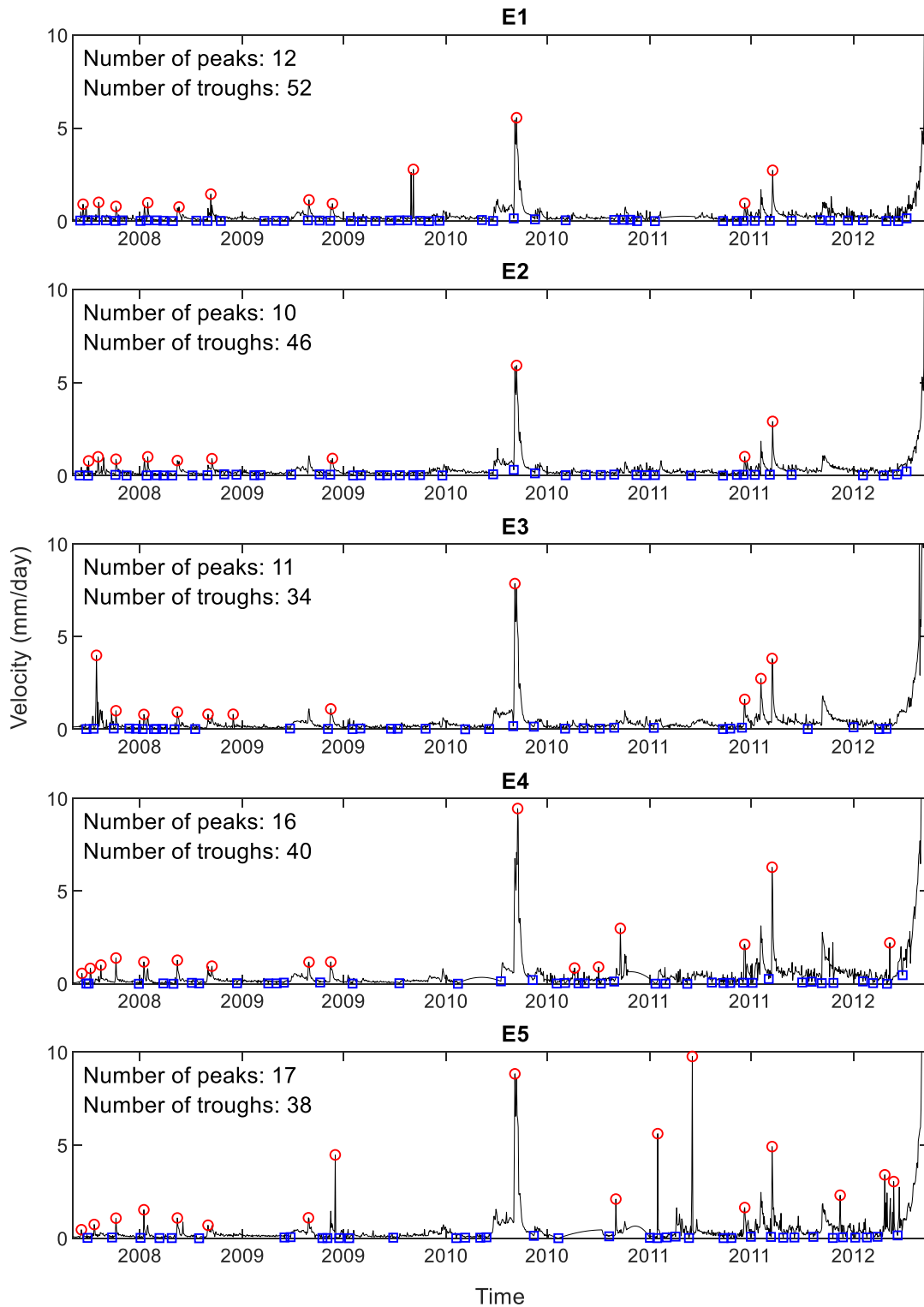
Supplementary Fig. 5 Pre-peak (open symbols) acceleration and post-peak (colored symbols) relaxation of Type IV exogenous-critical peaks. Variation of normalized velocity as a function of pre/post-peak time for the five extensometers E1-E5.



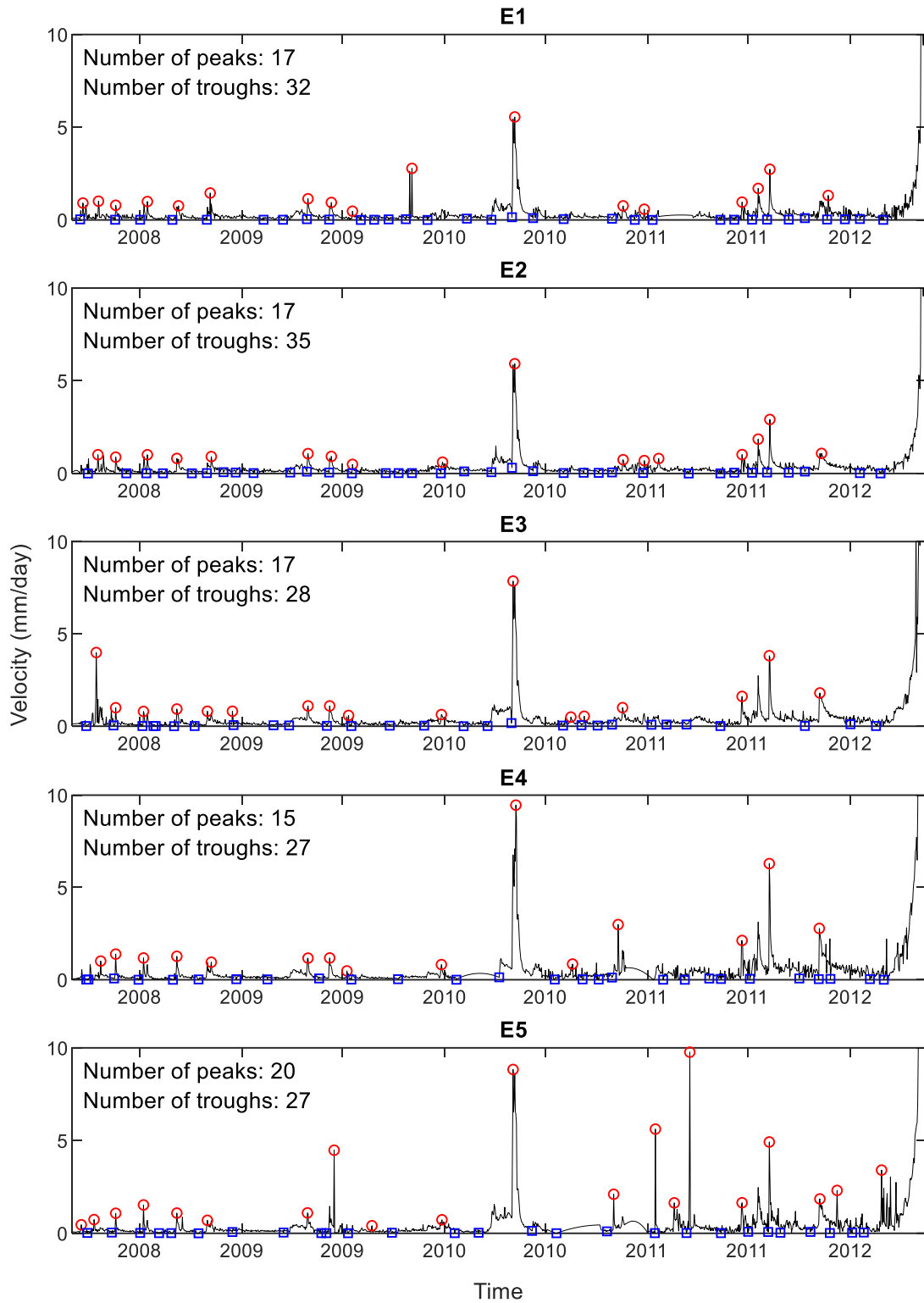
Supplementary Fig. 6 Time series of daily slope velocities recorded by the five extensometers E1-E5 (from top to bottom) instrumented at the Preonzo landslide, Switzerland. Peaks and troughs are marked by circles and squares, respectively. Each peak (respectively trough) is qualified as a local maximum (respectively minimum) over a 20-day time window which is at least $k = 2.5$ times larger (respectively smaller) than the average velocity over a 2-month time window.



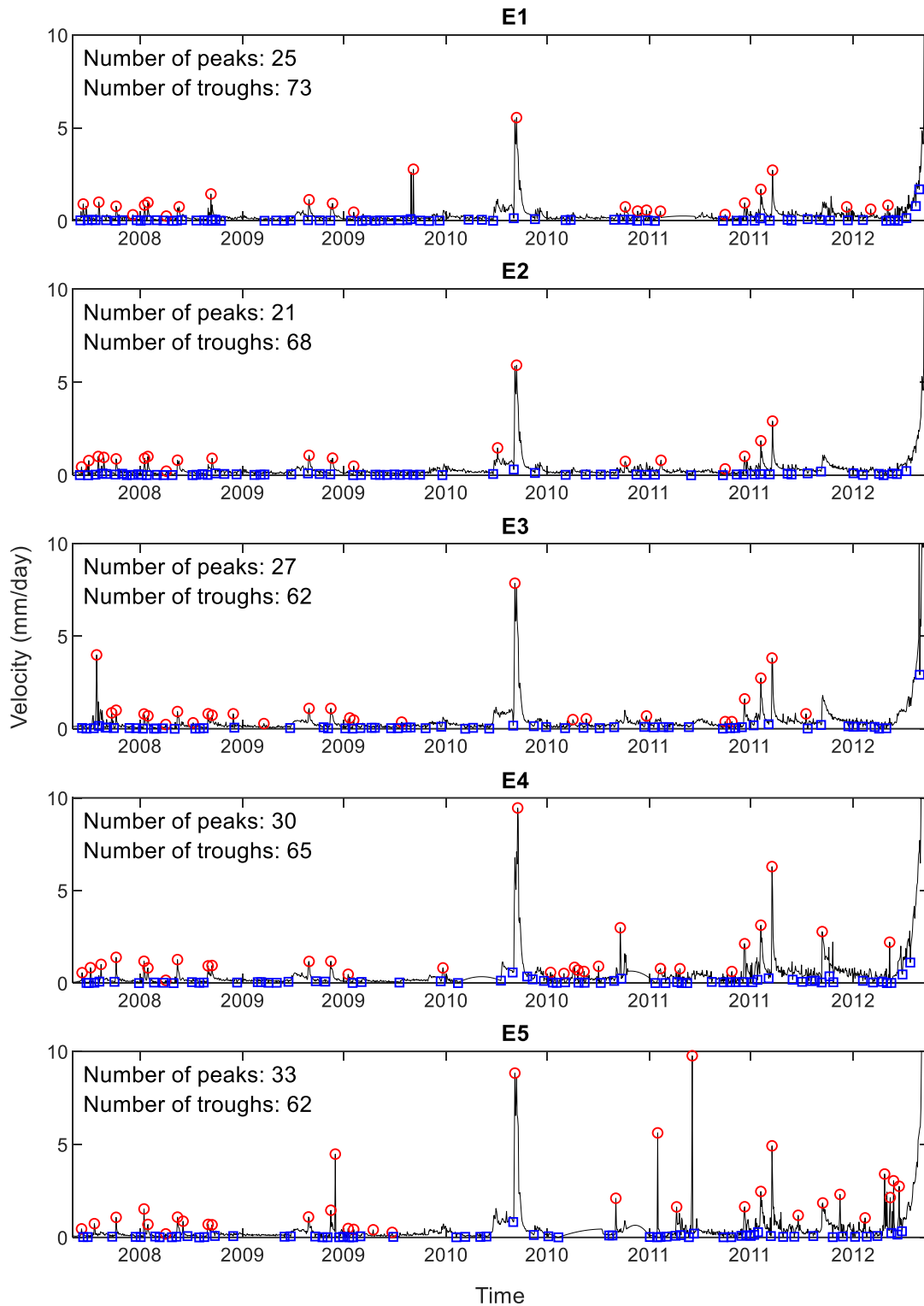
Supplementary Fig. 7 Time series of daily slope velocities recorded by the five extensometers E1-E5 (from top to bottom) instrumented at the Preonzo landslide, Switzerland. Peaks and troughs are marked by circles and squares, respectively. Each peak (respectively trough) is qualified as a local maximum (respectively minimum) over a 20-day time window which is at least $k = 1.5$ times larger (respectively smaller) than the average velocity over a 2-month time window.



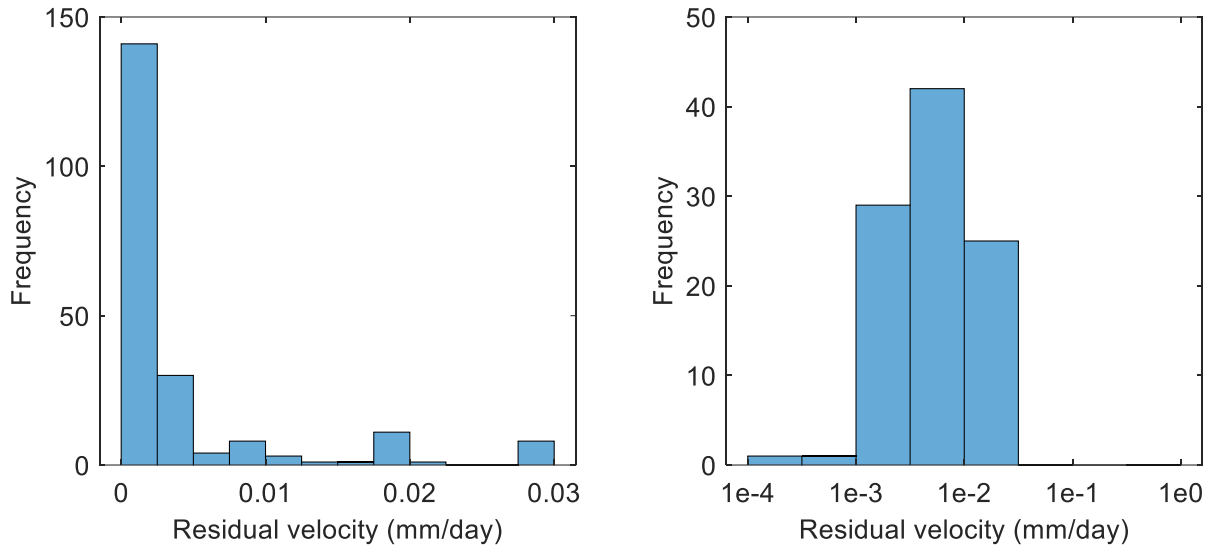
Supplementary Fig. 8 Time series of daily slope velocities recorded by the five extensometers E1-E5 (from top to bottom) instrumented at the Preonzo landslide, Switzerland. Peaks and troughs are marked by circles and squares, respectively. Each peak (respectively trough) is qualified as a local maximum (respectively minimum) over a 20-day time window which is at least $k = 3.5$ times larger (respectively smaller) than the average velocity over a 2-month time window.



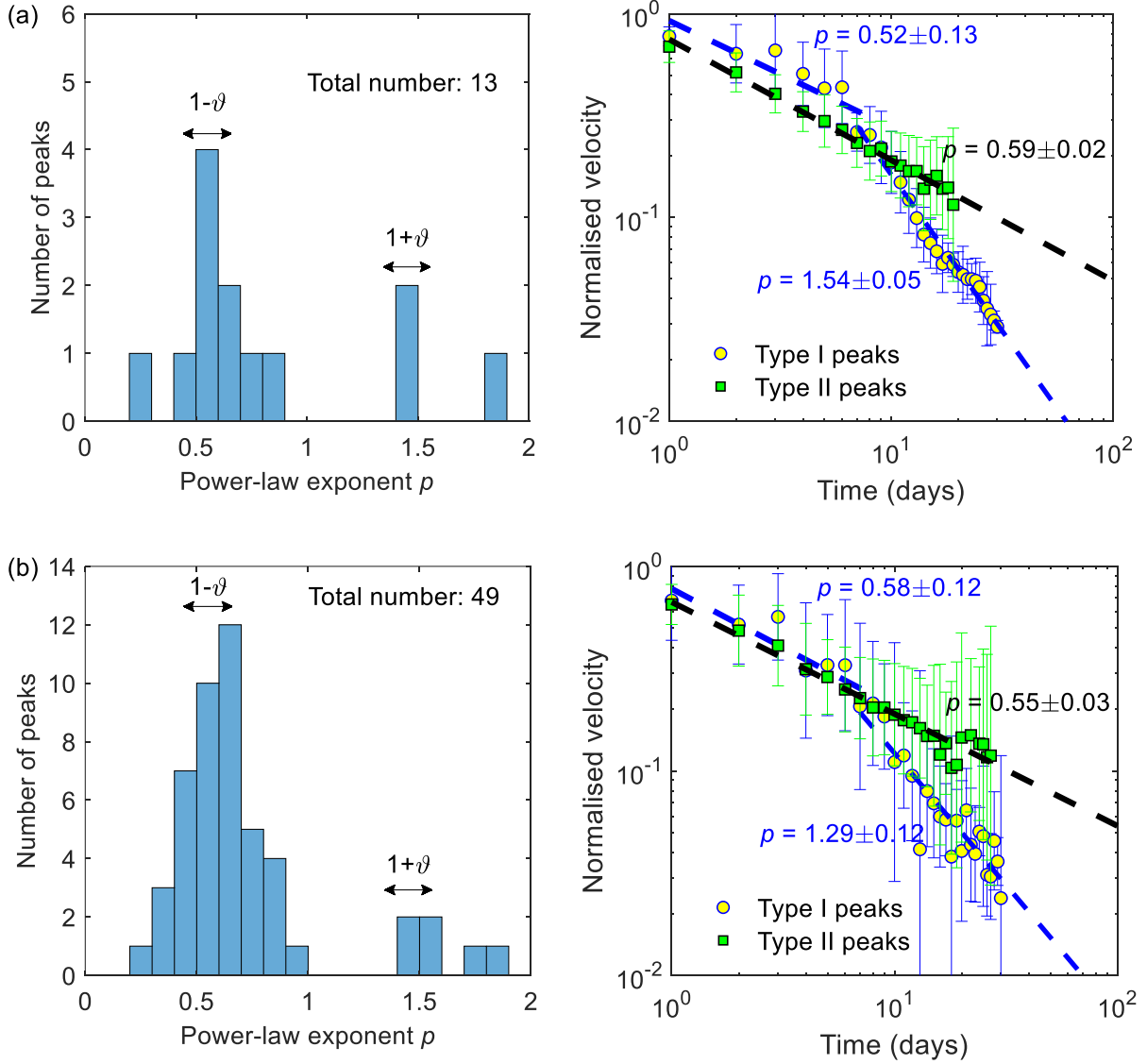
Supplementary Fig. 9 Time series of daily slope velocities recorded by the five extensometers E1-E5 (from top to bottom) instrumented at the Preonzo landslide, Switzerland. Peaks and troughs are marked by circles and squares, respectively. Each peak (respectively trough) is qualified as a local maximum (respectively minimum) over a 40-day time window which is at least $k = 2.5$ times larger (respectively smaller) than the average velocity over a 4-month time window.



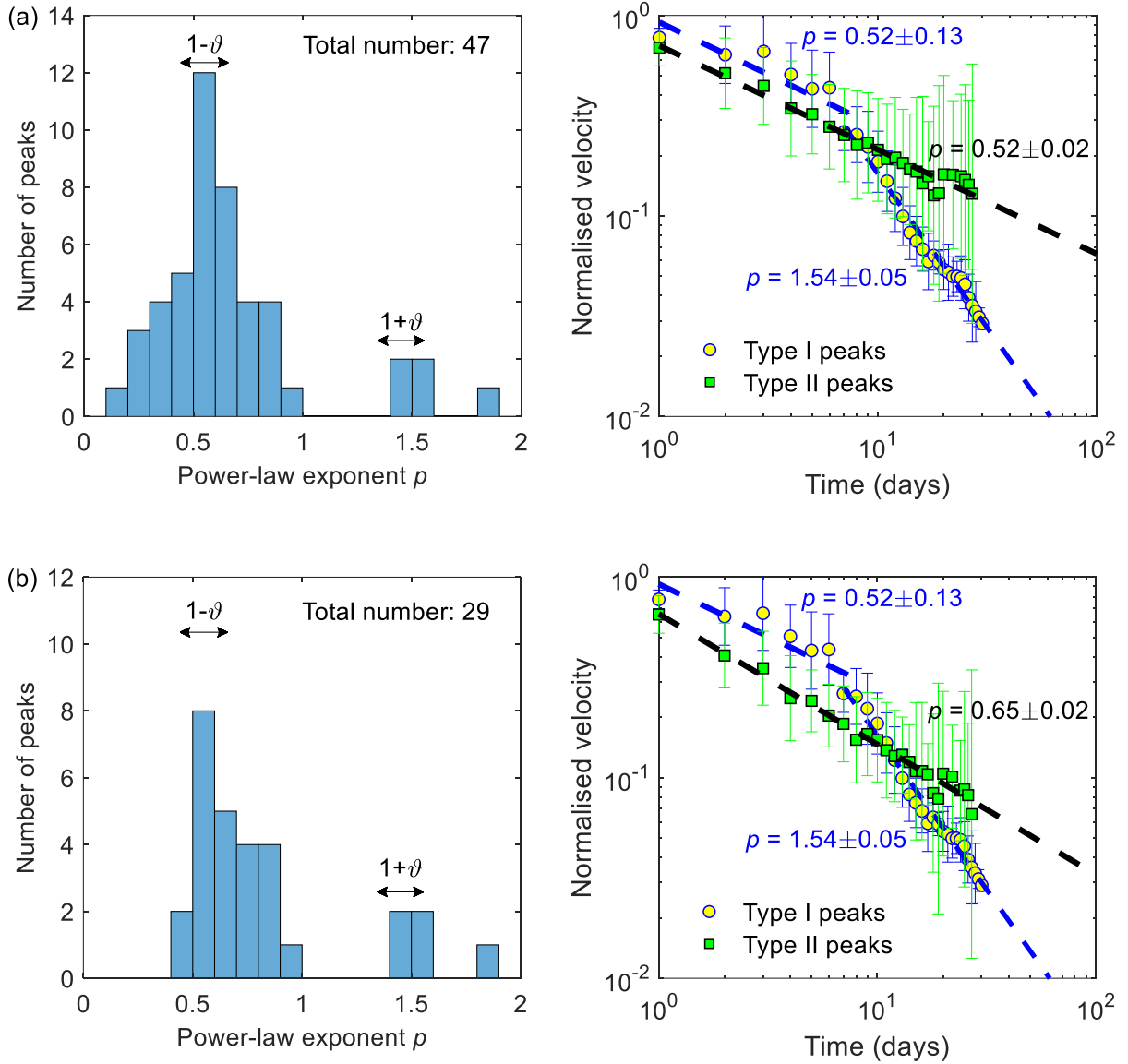
Supplementary Fig. 10 Time series of daily slope velocities recorded by the five extensometers E1-E5 (from top to bottom) instrumented at the Preonzo landslide, Switzerland. Peaks and troughs are marked by circles and squares, respectively. Each peak (respectively trough) is qualified as a local maximum (respectively minimum) over a 10-day time window which is at least $k = 2.5$ times larger (respectively smaller) than the average velocity over a 1-month time window.



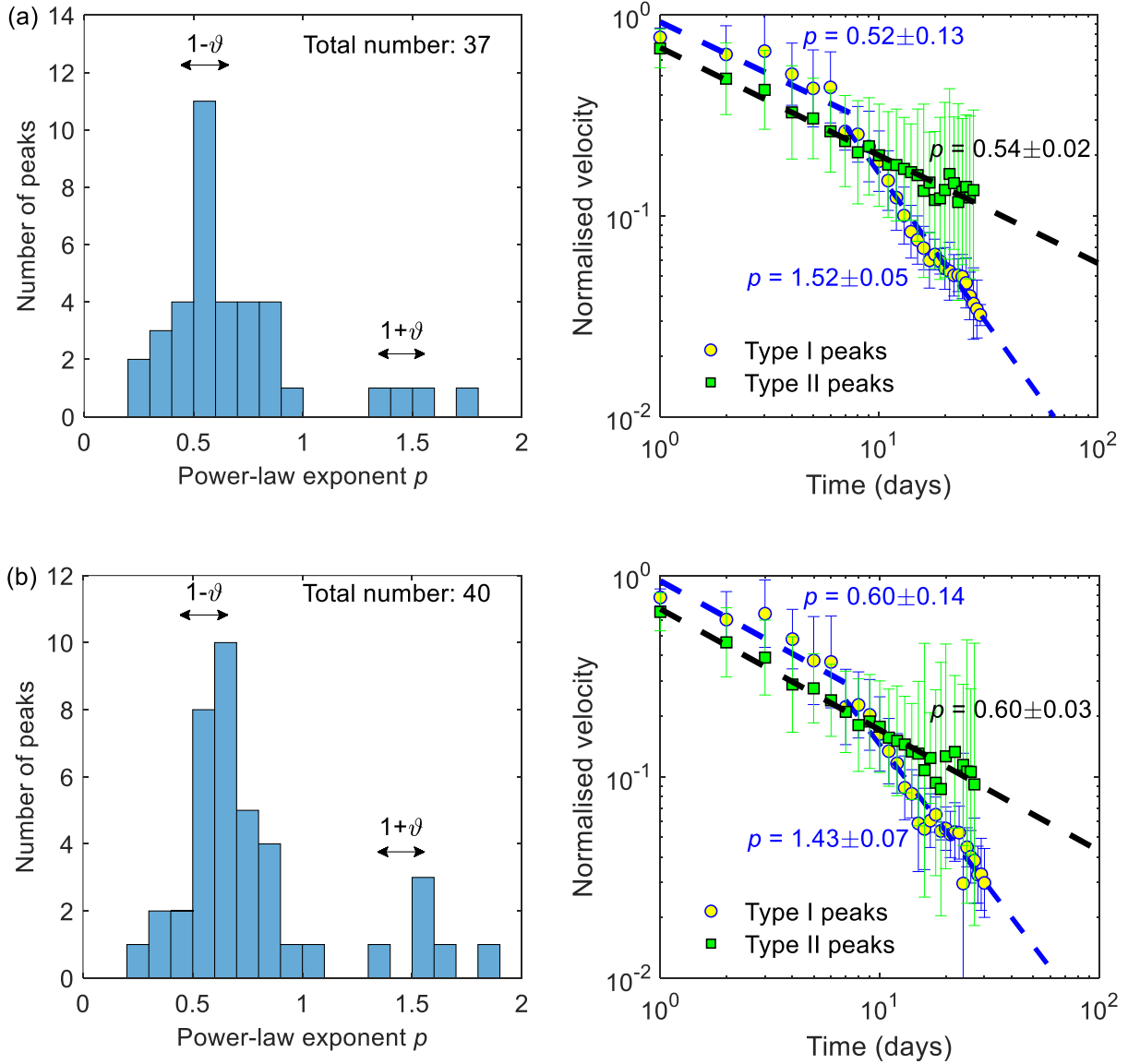
Supplementary Fig. 11 Histogram of slope residual velocities. Data are plotted in a linear scale (left) and a logarithmic scale (right).



Supplementary Fig. 12 Post-peak relaxation properties associated with detected peaks in the velocity time series. Left: histogram of the power law exponents p for post-peak velocity relaxation. Right: ensemble averaged relaxation of Type I (exogenous-subcritical) and Type II (exogenous-critical) peaks. Here, a peak is qualified as a local maximum over a 20-day time window which is at least $k = 2.5$ times larger than the average velocity over a 2-month time window, while the coefficient of determination for the fitting should meet **a** $R^2 > 0.9$ or **b** $R^2 > 0.7$.



Supplementary Fig. 13 Post-peak relaxation properties associated with detected peaks in the velocity time series. Left: histogram of the power law exponents p for post-peak velocity relaxation. Right: ensemble averaged relaxation of Type I (exogenous-subcritical) and Type II (exogenous-critical) peaks. Here, a peak is qualified as a local maximum over a 20-day time window which is at least **a** $k = 1.5$ or **b** $k = 3.5$ times larger than the average velocity over a 2-month time window, while the coefficient of determination for the fitting should meet $R^2 > 0.8$.



Supplementary Fig. 14 Post-peak relaxation properties associated with detected peaks in the velocity time series. Left: histogram of the power law exponents p for post-peak velocity relaxation. Right: ensemble averaged relaxation of Type I (exogenous-subcritical) and Type II (exogenous-critical) peaks. Here, a peak is qualified as a local maximum over a (a) 40-day or (b) 10-day time window which is at least $k = 2.5$ times larger than the average velocity over a a 4-month or **b** 1-month time window, while the coefficient of determination for the fitting should meet $R^2 > 0.8$.